Univerzita Karlova v Praze
Matematicko-fyzikální fakulta

DISERTAČNÍ PRÁCE

Boris Pokorný

Měření difrakční produkce dvou jetů v hloubkově nepružném rozptylu na urychlovači HERA

Ústav částicové a jaderné fyziky

Vedoucí práce: RNDr. Alice Valkárová, DrSc.

Studijní program: Subjaderná fyzika (F9)

Charles University in Prague
Faculty of Mathematics and Physics

DOCTORAL THESIS

Boris Pokorný

Measurement of Diffractive Dijet Production in Deep Inelastic Scattering at HERA Collider

Institute of Particle and Nuclear Physics

Supervisor: RNDr. Alice Valkárová,DrSc.

Field of Study: Physics, Nuclear and Particle Physics

Acknowledgments

I'd like to express my gratitude to all who have made this thesis possible. Special thanks belongs to my supervisor Alice Valkárová for guiding this work from the very beginning throughout the years. Her advice stemming from wide experience and deep insight was inspiring and encouraging.

This analysis could be hardly accomplished without many knowledgeable discussions with colleagues from the H1 experiment. Particularly I'd like to thank to Karel Černý for his preserving and instantious help especially within our private talks. Thanks belongs to Radek Žlebčík and Daniel Britzger for introducing me into problems of NLO calculations. I'm grateful to H1 people for sharing their expertise at collaboration meetings in Hamburg that were vitally important for the progress in the analysis.

This work has been enabled thanks to funding of the Department of Particle Physics in Prague and the grant of Ministry of Education, Youth and Sports INGO LA09042.

Prohlašuji, že svou disertační práci jsem napsal samostatně a výhradně s použitím citovaných pramenů. Souhlasím se zapůjčováním práce.

V Praze dne

Abstract

The diffractive production of two jets in deep inelastic $e^{\pm}p$ scattering is measured in the kinematic region of photon virtuality $4 < Q^2 < 80$ GeV^2, inelasticity $0.1 < y < 0.7$, momentum fraction $x_{I\!P} < 0.03$, proton vertex momentum transfer $|t| < 1$ and mass of a dissociative baryonic system $M_Y < 1.6$ GeV. Diffractive events are identified with the large rapidity gap technique. Integrated and single differential cross sections are measured for jets of transverse momenta $p^*_{T1} > 5.5$ GeV and $p^*_{T2} > 4.0$ GeV and pseudorapidities $-3 < \eta^*_{1,2} < 0$. The data were collected by the H1 experiment at the HERA collider in years 2005-2007, corresponding to an integrated luminosity of 283.7 pb^{-1}. The measurements are compared with NLO predictions based on the DGLAP parton evolution.

Contents

Chapter 1

Introduction

In the past decades a theoretical framework describing interactions of all known elementary particles has been developed. The Standard Model (SM) of particle physics emerged in 1970s and nowadays it includes a unified theory of electromagnetic and weak interactions as well as description of strong interactions. The predictive power of SM has been manifested by results of many experiments. High energy available at the Large Hadron Collider (LHC) allows to explore the Higgs sector and confirm thus the validity of SM completely. Theories going beyond SM face the challenge to unify the electroweak and strong force or to explain phenomena like neutrino oscillations or dark matter.

Dynamics of strong interactions, Quantum Chromo Dynamics (QCD), is formulated by means of a non-abelian gauged field theory. In QCD, constituent quarks of the additive quark model play role of basic interacting fermions whereas the strong force carriers, gluons, are introduced in order to meet the fundamental symmetry requirements. The non-abelian nature of QCD reveals predictions of phenomena like the quark confinement or vanishing of the strong force at small distances (asymptotic freedom). Application of the perturbation theory is limited in QCD and consequently, internal structure of hadrons ought to be parametrized by means of universal structure functions.

Structure of hadrons is experimentally well accessible in lepton-hadron interactions where the scattered lepton provides the information for the structure functions determination.

A class of processes where the scattering occurs at low momentum transfer is known as diffraction. The applicability of the perturbation theory is conditioned by introducing a color neutral exchange, pomeron, which has partonic structure. Structure functions of the pomeron are defined in analogy to the nucleon structure functions. A significant fraction of the observed cross section of the *ep* scattering at the HERA collider stems from the diffractive scattering [1, 2] and the collected data are suitable for the extraction of the pomeron parton densities. Based on the measured pomeron structure, the production of particular diffractive final states, e.g. jet or charm production, can be predicted within the uncertainties of the data.

Gluon content of the pomeron can be determined either from measurements of scaling violations of the inclusive diffractive structure functions or from a direct measurement of the cross section of gluon induced processes. A typical diffractive process sensitive to the gluon density is the production of two jets.

The next chapter gives a brief overview of the current understanding of the hadronic structure in terms of QCD and the quark parton model. In Chapter 3, the experimental facility of the HERA collider and H1 detector is briefly described. The course of the presented analysis including the data selection, monte carlo simulation and NLO calculation is described in detail in Chapter 4. In Chapter 5, the measured cross section of the diffractive dijet production is presented.

Chapter 2

Theoretical Overview

This chapter summarizes theoretical concepts that underlay the presented measurements.

2.1 Deep Inelastic Scattering

Interactions observed at HERA are dominated by scattering of a lepton (electron or positron) on a proton

$$l(k) + p(P) \to l'(k') + X \tag{2.1}$$

where $k(k')$ denotes the momentum of the incoming (out-coming) electron (positron), P is the momentum of the incoming proton and X is an arbitrary hadronic final state. These interactions are divided into two classes according to charge of a gauge boson exchanged between the lepton and the proton:

- Neutral Current (NC) processes where γ or Z_0 is exchanged and the charge of the lepton is conserved $l = l'$
- Charged Current (CC) processes with $W^{\pm}$ exchange and l' is different from l by one unit of charge.

Only NC processes are studied in this work and the term electron denotes either electron or positron in what follows. Energies available at HERA are too low for the Z_0 production hence the NC processes of interest are mediated exclusively by the γ exchange.

2.1.1 Kinematics

The kinematics of the electron-proton scattering can be described in terms of the following Lorentz invariant variables:

$$s = (k+P)^2 \tag{2.2}$$

$$Q^2 = -q^2 = -(k-k')^2 \tag{2.3}$$

$$x = \frac{Q^2}{Pq} \tag{2.4}$$

$$y = \frac{qP}{kP} = \frac{E_{lab} - E'_{lab}}{E_{lab}} \tag{2.5}$$

$$W^2 = (q+P)^2 \tag{2.6}$$

where s is interpreted as the squared energy in the Central Mass System (CMS) and Q^2 as the squared momentum transfer from the incoming to out-coming electron. Interpretation of x as the proton momentum fraction carried by the struck parton is explained in section 2.1.3. The inelasticity y measures the relative energy loss of the electron in the laboratory frame and W^2 represents the squared invariant mass of the system X. Not all of the introduced quantities are independent - any pair of Q^2, x, y fully describes the kinematics.

The electron-proton scattering is further classified based on the momentum transfer Q^2. Processes with the momentum transfer higher than the proton mass, $Q^2 \gg 1\text{GeV}^2$, are referred to as Deep Inelastic Scattering (DIS) while the low momentum transfer scattering, $Q^2 \sim 0$, is referred to as Photoproduction (PHP).

2.1.2 Cross Section of *ep* Scattering

Elastic scattering of electrons on point-like protons can be described to the lowest order of perturbative QED by a one photon exchange diagram (Figure 2.1 a)). Denoting M_p the mass of the proton, the differential cross section reads

$$\frac{d\sigma}{dQ^2} = \frac{2\pi\alpha^2}{Q^4}[1 + (1-y)^2 - \frac{M_p^2 y}{kP}] \tag{2.7}$$

The above formula is valid for a lepton scattering on an arbitrary spin 1/2 point-like particle. The differential cross section of scattering of a lepton on a point-like boson of mass M_B has form

$$\frac{d\sigma}{dQ^2} = \frac{2\pi\alpha^2}{Q^4}[1 - y - \frac{M_B^2 y}{kP}] \tag{2.8}$$

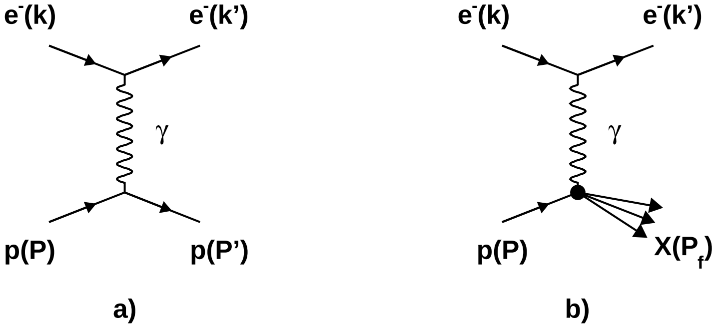

Figure 2.1: Scattering of electron on point-like proton a). Scattering of electron on realistic proton b).

In case of the real proton, the point-like coupling in the lower vertex in Figure 2.1 is replaced with a tensor that contains unknown functions reflecting the internal structure of the proton. The fundamental requirements of Lorentz invariance, gauge invariance, parity conservation and unitarity lead to the cross section of the inelastic electron-proton scattering

$$\frac{d^2\sigma}{dQ^2dx} = \frac{2\pi\alpha^2}{Q^4x}[(1-y-\frac{M_P^2xy}{s})F_2(x,Q^2)+y^2xF_1(x,Q^2)] \tag{2.9}$$

where $F_1(x,Q^2)$, $F_2(x,Q^2)$ are structure functions of proton, sometimes also referred to as electromagnetic formfactors of the proton.

2.1.3 Quark Parton Model

The basic assumption of the Quark Parton Model (QPM) is to view a proton as a compound object consisting of point-like charged constituents - partons. The cross section of *ep* scattering can be written as an incoherent sum of cross sections of elastic electron-parton scattering.

The QPM is is formulated in the infinite momentum frame and assuming the collision is deeply inelastic with $Q^2 \gg M_P^2$. In this frame, parton transverse momenta are negligible with respect to the proton momentum, hence the parton fourmomentum can be expressed as $p = \xi P$. The fraction ξ is identified with the invariant $x = Q^2/Pq$ since the momentum conservation law for the electron-parton scattering yields $2pq = Q^2$ (taking zero mass of partons).

In the infinite momentum frame, relation 2.9 is left with one structure function only:

$$\frac{d^2\sigma}{dQ^2dx} = \frac{2\pi\alpha^2}{Q^4}\frac{F_2(x,Q^2)}{x} \tag{2.10}$$

since $y \to 0$ for $s \to \infty$ at fixed Q^2. The same limit for both 2.7 and 2.8 leads to

$$\frac{d\sigma}{dQ^2} = \frac{4\pi\alpha^2 e_p^2}{Q^4} \tag{2.11}$$

where e_p is charge of the target particle. The cross section of electron-parton scattering does not depend on spin of partons in the infinite momentum frame and the structure function can be written as

$$F_2(x) = x\sum e_i^2 d_i(x) \tag{2.12}$$

where probability densities $d_i(x)$ express the probability of finding a parton of type i with charge e_i and proton momentum fraction x.

Spin of partons can be examined through the Callan-Gross relation [3], which relates the structure functions F_1 and F_2

$$F_2(x) = 2xF_1(x) \tag{2.13}$$

Inserting the Callan-Gross relation into 2.9 yields

$$\frac{d^2\sigma}{dQ^2dx} = \frac{2\pi\alpha^2}{Q^4x}[1+(1-y)^2]F_2(x) \tag{2.14}$$

If the Callan-Gross relation is valid the constituent partons ought to be spin 1/2 particles. This can be seen comparing the above expression with the electron-fermion elastic scattering cross section 2.7. The experimental proof of 2.14 confirms that partons are indeed 1/2 spin particles. It is than natural to associate the partons with the constituent quarks of the additive quark model. The distribution functions $d_i(x)$ appearing in 2.12 are identified with the quark and anti-quark probability distributions, $q_i(x)$ and $\bar{q}_i(x)$, with i indexing now the quark flavors:

$$F_2(x) = x\sum e_i^2(q_i(x) + \bar{q}_i(x)) \tag{2.15}$$

The identification of partons with quarks is not straightforward since individual integrals over q_i, $\bar{q}_i$ are divergent. Finite integrals can be achieved for so called valence distributions defined as $q_{val}(x) = q(x) - \bar{q}(x)$. Only the valence distributions can be consistently identified with the quarks of the additive model. The remaining distributions are known as sea quarks and satisfy $q_{sea}(x) = \bar{q}_{sea}$. The sea quarks originate from the gluon radiation and $q\bar{q}$ pairs production.

2.2 Quantum Chromodynamics

QCD is the underlying gauge field theory of strong interactions. The gauge transformation group is SU(3) and QCD is thus characterized as a non-abelian theory. The basic interacting fermions of QCD are quarks which are ascribed a new degree of freedom, known as color charge. Quarks thus may exist in three different states, conventionally labeled as red, green and blue. The intermediate bosons of QCD are gluons which are massless neutral particles carrying color charge.

2.2.1 Renormalization

Besides the basic symmetry properties, the exact form of the QCD Lagrangian follows the requirement of renormalizability. Renormalization is a procedure that redefines a gauge field theory, so that relevant predictions can be achieved via perturbative calculations. The requirement of renormalizability is essential for any realistic theory.

Perturbative QCD (pQCD) assumes that any observable can be expanded in powers of strong coupling α_s with coefficients evaluated according to corresponding Feynman diagrams. Higher order corrections contain loops where momentum integration leads to infinite contributions. These so called Ultra Violet (UV) divergences can be eliminated by transforming mass, charge and fields acquiring thus a redefined theory where the infinities are absorbed in the renormalized coupling α_s. The original quantities (before the renormalization) are referred to as bare mass, bare charge, etc.

There are several ways to achieve a renormalized theory; a renormalization scheme refers to a particular choice of one of them. Modified minimal subtraction (MS) [4] is a frequently used renormalization scheme based on so called dimensional regularization [5]. A renormalization scale μ_r is introduced in MS as an arbitrary parameter constraining the area where the subtraction is performed. It is important for any physics observable $R(\mu_r)$ not to be explicitly dependent from the arbitrary scale μ_r. This dependence must be compensated by the α_s dependence on μ_r (running α_s) which is expressed by the Renormalization Group Equation (RGE) [6]:

$$\mu_r^2(\frac{\partial R}{\partial \mu_r^2} + \frac{\partial \alpha_s}{\partial \mu_r^2}\frac{\partial R}{\partial \alpha_s}) = 0 \tag{2.16}$$

Writing down the above equation it is implicitly assumed that quarks are massless and $R(\mu_r)$ is a dimensionless quantity. The explicit dependence of

α_s on μ_r^2 follows from the RGE and can be obtained through the expansion

$$\mu_r \frac{\mathrm{d}\alpha_s}{\mathrm{d}\mu_r} = -\alpha_s \sum_{n=0}^{\infty} \beta_n \left(\frac{\alpha_s}{4\pi}\right)^{n+1} \tag{2.17}$$

where coefficients β_n are known for $n < 4$ and the first two of them can be expressed in terms of number of quark flavors (n_f) and colors (n_c):

$$\beta_0 = \frac{11n_c - 2n_f}{6} \tag{2.18}$$

$$\beta_1 = \frac{51n_c - 19n_f}{22n_c - 4n_f} \tag{2.19}$$

The solution of 2.17 up to the order $O(\alpha_s^2)$ takes form

$$\alpha_s(\mu_r) = \frac{4\pi}{\beta_0 ln(\mu_r^2/\Lambda^2)}[1 - \frac{2\beta_1}{\beta_0^2}\frac{ln(ln(\mu_r^2/\Lambda^2))}{ln(\mu_r^2/\Lambda^2)}] \tag{2.20}$$

where Λ is introduced as a free parameter of the theory and has to be determined from measurements. the value of Λ can be enumerated from the measured value of $\alpha_s(M_Z^2) = 0.118$, with M_Z being the mass of the Z boson. The parameter Λ constrains the applicability of the pQCD. Taking into account that $\alpha_s \to \infty$ for $\mu_r \to \Lambda$, the perturbation expansion can be readily applied only for $\mu_r \gg \Lambda$. The growth of α_s at small scales (i.e. large distances) leads to the concept of confinement. Although the perturbative approach breaks down at these scales, lattice QCD explains the confinement as a consequence of non-linearities of the $SU(3)$ gauge fields [7]. On the other hand, the large scales limit $\alpha_s \to 0$ as $\mu_r \to \infty$ justifies the assumption of quasi-free quarks in the original QPM. The vanishing of the couplant at large scales, referred to as asymptotic freedom, is a general property of non-abelian gauge theories.

2.2.2 Factorization Theorem

The UV divergences can be absorbed in the running couplant α_s in course of the renormalization procedure but there still remains a class of divergences stemming from collinear parton emissions. These divergences can be factored out of the hard scattering cross-section and absorbed into parton distribution functions (PDF) $f_i(\xi, \mu_f^2, \alpha_s(\mu_r))$. The factorization theorem in DIS can be written as [8]

$$\sigma(x, Q^2) = \sum_{i=q,\bar{q},g} \int_x^1 \frac{\mathrm{d}\xi}{\xi} f_i(\xi, \mu_f^2, \alpha_s(\mu_r)) \hat{\sigma}_i(\frac{x}{\xi}, \frac{Q^2}{\mu_r^2}, \frac{\mu_r^2}{\mu_f^2}, \alpha_s(\mu_r)) \tag{2.21}$$

with $\hat{\sigma_i}$ being the partonic cross section calculable in pQCD. PDFs are dependent on the factorization scale μ_f and renormalization scheme through α_s and the straightforward probability interpretation is no more possible as for their bare counterparts 2.12. However, the PDF are scale independent in the leading order (LO) and $f_i(x)dx$ stands for probability to find a parton type i in the momentum fraction interval $(x, x + dx)$.

Partons emitted with momentum below the factorization scale μ_f are treated as a part of PDF. The factorization scale μ_f thus has a meaning of a threshold above which the pQCD is applicable.

2.2.3 Evolution of Parton Distributions

PDFs acquire additional dependence on factorization scale μ_f as a consequence of non-perturbative long distance effects originating from the initial state of bounded partons. The physics interpretation stipulates the requirement that parton densities, summed in all orders of pQCD, are μ_f independent. The finite order PDF μ_f dependence thus cannot be arbitrary but obeys analogous restriction as expressed in RGE 2.16. The corresponding differential equation solution is available in various approximations relying on neglecting certain type of terms in perturbation expansions. The approximation neglecting the logarithmic terms leads to a set of integro-differential equations referred to as Dokshitzer, Gribov, Lipatov, Altarelli, Parisi (DGLAP) evolution equations [9, 10, 11]:

$$\frac{\mathrm{d}f_q(x,\mu_f^2)}{\mathrm{d}\ln\mu_f^2} = \frac{\alpha_s(\mu_r)}{2\pi}\int_x^1 \frac{\mathrm{d}y}{y}[P_{qq}(\frac{x}{y})f_q(y,\mu_f^2) + P_{qg}(\frac{x}{y})f_g(y,\mu_f^2)] \tag{2.22}$$

$$\frac{\mathrm{d}f_g(x,\mu_f^2)}{\mathrm{d}\ln\mu_f^2} = \frac{\alpha_s(\mu_r)}{2\pi}\int_x^1 \frac{\mathrm{d}y}{y}[P_{gg}(\frac{x}{y})f_g(y,\mu_f^2) + P_{gq}(\frac{x}{y})f_g(y,\mu_f^2)] \tag{2.23}$$

Splitting functions $P_{ij}(z)$ describe the probability that a parton of type i and momentum fraction z radiates another parton of type j carrying the momentum fraction $(1 - z)$. An expansion of the splitting functions in powers of $\alpha_s(\mu_r)$ with coefficients calculable in pQCD can be written

$$P_{ij}(z,\alpha_s) = \sum_{n=0}^{\infty}\left(\frac{\alpha_s}{2\pi}\right)^n P_{ij}^{(n-1)}(z) \tag{2.24}$$

The splitting functions are known up to NNLO, e.g. $O(\alpha_s^2)$. In the LO, they take form

$$P^0_{qq}(z) = \frac{4}{3}\frac{1+z^2}{1-z} \tag{2.25}$$

$$P^0_{qg}(z) = \frac{1}{2}(z^2 + (1-z^2)) \tag{2.26}$$

$$P^0_{gg}(z) = 6(\frac{z}{1-z} + \frac{1-z}{z} + z(1-z)) \tag{2.27}$$

$$P^0_{gq}(z) = \frac{4}{3}\frac{1+(1-z)^2}{z} \tag{2.28}$$

The vertexes corresponding to individual LO splitting functions are sketched

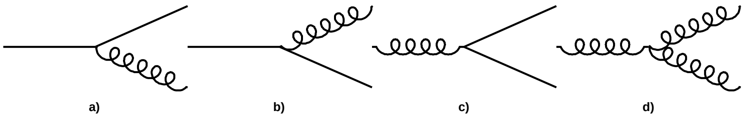

Figure 2.2: Feynman diagrams corresponding to splitting functions P_{qq} a), P_{qg} b), P_{gq} c) and P_{gg} d).

in Figure 2.2. Given an initial value $f_i(x, \mu^2_{f0})$, the DGLAP equations thus allow to determine the parton density at any scale μ_f. The parton density evolves via a subsequent emission of partons from the struck parton. The radiated partons are ordered in their longitudinal momenta $x_1 > x_2 > ... > x_n = x$ and strongly ordered in their transverse momenta $k_{T1} \ll k_{T2} \ll ... \ll k_{Tn} = \mu^2_f$. Figure 2.3 shows a diagram corresponding to gluon emission, so called gluon ladder. A particular choice of the factorization scale μ_f has to be done for the purpose of the experimental PDF determination. Concerning general DIS, the choice $\mu^2_f = Q^2$ provides a hard enough scale.

2.2.4 Hadronization

Only colorless hadrons have been observed so far in nature, which coincides well with the phenomenon of confinement. Final state partons are converted into observable hadrons as distances between them increase. This process is known as hadronization. Due to the low scales involved, the hadronization is a non-perturbative effect and relevant predictions cannot be calculated from the first principles. Various phenomenological models are used instead [12].

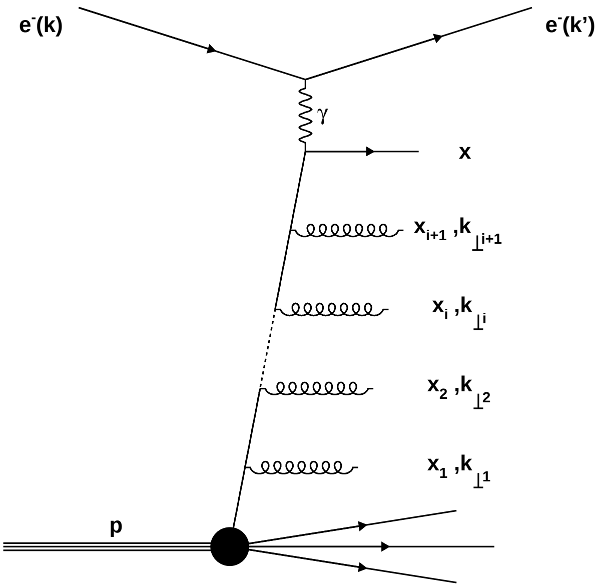

Figure 2.3: Parton density evolution in the DGLAP picture - a gluon ladder diagram.

2.3 Diffraction

The term diffractive scattering is, in general, related to elastic hadron-hadron scattering. Low scales of these soft processes do not allow for application of the pQCD and phenomenological approach is necessary.

2.3.1 Regge Model and Pomeron

A two body interaction $a + b \to c + d$ was originally modeled as a One Pion Exchange (OPE). However, there are processes, for which the OPE collides with the quantum number conservation laws. For example a πp elastic scattering can not be realized through the pion exchange due to the G-parity conservation. The OPE applicability is further restricted by Froissart bound on the cross section σ [14]

$$\sigma \leq \frac{\pi}{m_\pi^2} \ln^2 s \tag{2.29}$$

where $s = (p_a + p_b)^2$ is the central mass energy squared. This bound is violated if the exchanged meson spin is higher than one and the OPE is thus not suitable to describe high energy behavior of the cross section.

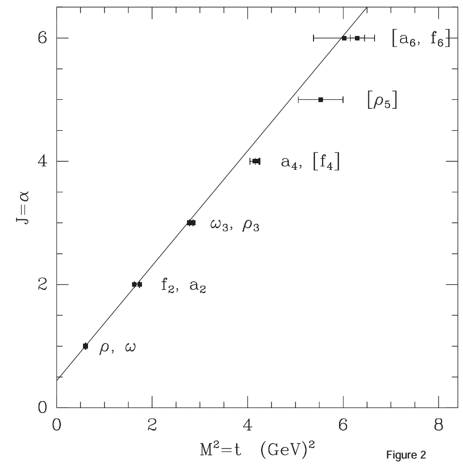

Figure 2.4: Chew-Frautschi plot - low mass meson states orbital momentum J versus mass squared [13].

A theory formulated by Tullio Regge [15, 16] describes the interaction as an exchange not only a single meson but rather a whole multitude of mesons called Regge trajectories or Reggeons. The Regge trajectories can be illustrated in J, M^2 plane where meson states of different angular momentum J and mass M are situated at the same line (Figure 2.4). In the region of high energies and low scattering angles (so called Regge limit), $s \ll t$, the transition amplitude $\mathcal{A}(s,t)$ is found to be a sum of contributions from different trajectories [17]

$$\mathcal{A}(s,t) = \sum_i \beta_i^2(t) s^{\alpha_i(t)} \xi((\alpha_i(t))) \tag{2.30}$$

where $t = (p_a - p_b)^2$ is the energy transfer from a to b and $\xi((\alpha_i(t))$ is so called Regge signature. Trajectories are linear $\alpha(t) = \alpha' t + \alpha(0)$, where $\alpha(0)$ is the intercept of the trajectory. Assuming Reggeon exchange only, the differential cross section following from 2.30 can be parametrized as

$$\frac{d\sigma}{dt} = (\beta_a(t)\beta_b(t))^2 \left(\frac{s}{s_0}\right)^{2(\alpha(0)+\alpha' t-1)} \tag{2.31}$$

where s_0 refers to the hadronic scale and functions $\beta(t) = \beta_a(t)\beta_b(t)$ are related to form factors of hadrons entering the interaction. The hadronic scale is mostly taken at $s_0 \sim 1\mathrm{GeV}^2$ and parametrization $\beta_a(t) \propto e^{at}$ is widely used. The total cross section for the elastic scattering reads

$$\sigma_{tot} = \beta_a(0)\beta_b(0)s^{\alpha(0)-1} \tag{2.32}$$

Experimental data indicate $\alpha(0) > 1$ as the cross section increases with the central mass energy s, while $\alpha(0) < 0.6$ holds for all known meson trajectories. It is assumed that another term in 2.30, referred to as pomeron trajectory, plays role at higher energies. Although there are no known hadrons related to the pomeron trajectory, the relevant states carry vacuum quantum numbers ($C = P = +1$) and are being explored within the lattice QCD [18]. The assumption of the pomeron exchange leads to the Donnachie-Landshoff parametrization of the cross section

$$\sigma_{tot} = As^{\alpha_{I\!P}(0)-1} + Bs^{\alpha_{\mathbb{R}}(0)-1} \tag{2.33}$$

where $\alpha_{I\!P}$ ($\alpha_{I\!R}$) is the pomeron (Regge) trajectory intercept. The parameter A is fixed for both ab and $\bar{a}b$ reactions due to the photon-like coupling of the pomeron to quarks. The above parametrization fits accurately the total cross section of pp and $\bar{p}p$ interactions in the range from $\sqrt{s} = 5GeV$ to $\sqrt{s} = 1800GeV$ as illustrated in Figure 2.5. The pomeron trajectory was originally introduced by Gribov [19].

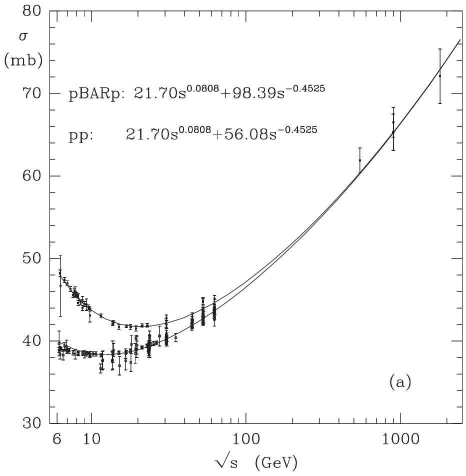

Figure 2.5: Comparison of total cross section of pp and $\bar{p}p$ interactions with Donnachie-Landshoff parametrization [13].

2.3.2 Diffraction in DIS

Diffractive DIS (DDIS) refers to processes $ep \rightarrow XY$ where final states X and Y are significantly separated in rapidity. This rapidity gap stems from an exchange of a colorless object - a color exchange would diminish any

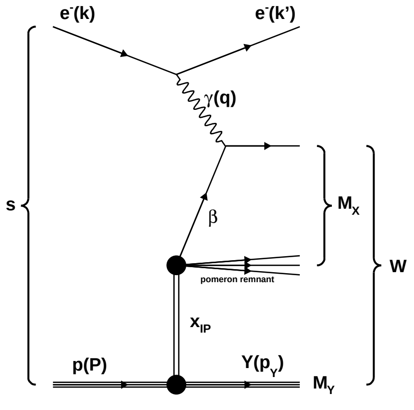

Figure 2.6: Schematic diagram of diffractive scattering in DIS.

clear difference in rapidity due to the strong force long-range behavior. The exchanged object is identified as pomeron.

The pomeron exchange kinematics is described by

$$x_{I\!P} = \frac{q.(P - p_Y)}{q.P} \tag{2.34}$$

which is interpreted as a longitudinal momentum fraction carried by pomeron with respect to the initial proton. Concerning a resolved pomeron model (ascribing the pomeron internal structure) the quantity

$$\beta = \frac{x}{x_{I\!P}} = \frac{Q^2}{2q.(P - p_Y)} \tag{2.35}$$

has the meaning of a longitudinal momentum fraction of the struck parton with respect to the pomeron. In analogy with 2.10, a diffractive structure function F_2^D is introduced and the cross section for the diffractive scattering reads

$$\frac{d^5\sigma}{dx_{I\!P}d\beta dQ^2 dM_Y dt} = \frac{4\pi\alpha_{em}^2}{\beta^2 Q^2}\Big(1 - y + \frac{y^2}{2(1 + R^{D(5)})}\Big)F_2^{D(5)} \tag{2.36}$$

where $R^{D(5)}$ denotes the ratio of longitudinal and transverse photon cross sections. The dependence on M_Y and t is integrated over and the structure function thus depends on three variables:

$$\frac{d\sigma}{dx_{I\!P}d\beta dQ^2} = \frac{4\pi\alpha_{em}^2}{\beta^2 Q^2}\Big(1 - y + \frac{y^2}{2}\Big)F_2^{D(3)}(x_{I\!P}, \beta, Q^2) \tag{2.37}$$

The ratio R^D is neglected in this analysis.

2.3.3 QCD Factorization and Pomeron Flux

The factorization theorem discussed in section 2.2.2 is essential for extracting universal parton densities in inclusive DIS. In this analogy, DDIS cross section is written as a convolution of the hard scattering cross section $\hat{\sigma}$ and the Diffractive Parton Densities (DPDF) $f_i^D(x, Q^2, x_{I\!P}, t)$

$$\sigma = \sum_i f_i^D(x, Q^2, x_{I\!P}, t) \otimes \hat{\sigma}(x, Q^2) \tag{2.38}$$

The QCD factorization in diffractive DIS interactions was proved by Collins [20]. Further more, DPDFs are reducible according to Regge factorization. Besides normalization, the DPDFs are independent from $x_{I\!P}$ and t and can be expressed in terms of $\beta = x/x_{I\!P}$ and Q^2

$$f_i^D(x, Q^2, x_{I\!P}, t) = f_{I\!P/p}(x_{I\!P}, t).f_{i/I\!P}(\beta, Q^2) \tag{2.39}$$

where $f_{I\!P/p}$ denotes the pomeron flux and $f_{i/I\!P}$ the pomeron parton density. The pomeron flux is interpreted as a probability to find a pomeron at certain $x_{I\!P}$ and t within the proton. In analogy with PDFs, the pomeron parton density has the meaning of probability to find a parton i within the pomeron and it is evolved according to DGLAP equations in DIS ($Q^2 > 4\text{GeV}^2$). Regge factorization is an assumption which was experimentally confirmed.

The DPDFs can be obtained from a DGLAP fit to the measured structure function F_2^D. Figure 2.7 shows DPDF for quarks and gluon as functions of the momentum fraction β as measured by H1 Collaboration [21].

2.3.4 Diffractive Jet Production in DIS

Measurement of cross section of inclusive diffractive scattering, allows to extract quark parton densities with a high accuracy. The gluon density is accessible through the measurement of scaling violations (Q^2 dependence of quark DPDF) but resulting uncertainties are considerably high, especially at the high relative momentum transfer β. Shortcomings of the gluon density extraction from the inclusive data can be avoided by a particular selection of the final state X ensuring thus a struck parton to be a gluon.

Productions of dijets in DDIS is dominated by Boson Gluon Fusion (BGF) as illustrated in Figure 2.8. Relevant quantity for the description

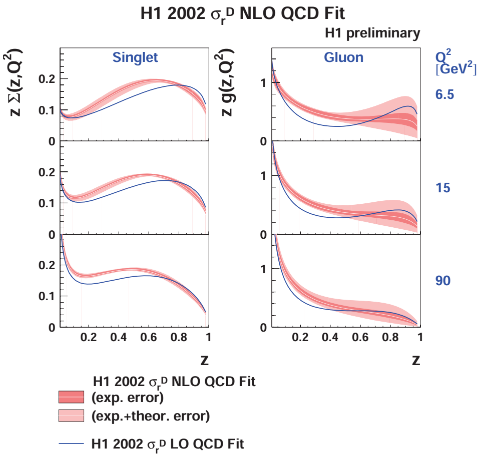

Figure 2.7: Diffractive parton distributions DGLAP fits to the H1 F_2^D data. Momentum fraction β is denoted as z. [21].

of kinematics is a longitudinal relative momentum of the gluon with respect to the pomeron:

$$z_{I\!P} = \frac{q.v}{q(P - p_Y)} = \frac{x}{x_{I\!P}} \qquad (2.40)$$

where v denotes a four-momentum of the gluon. The diffractive dijet cross section is then expressed in terms of the parton densities $f_{i/I\!P}(z_{I\!P}, \mu_f)$ and the pomeron flux $f_{I\!P}(x_{I\!P})$ convoluted with the hard scattering matrix elements.

Since the transverse momentum of the scattered electron is significant in DIS, the photon-proton axis does not coincide with the beam axis. The jets are reconstructed in γp center of mass system. In this frame, the jets are ordered in their transverse momenta p^*_{Ti} and jets with the highest and the second highest momentum are called the leading and subleading jet respectively. The transverse momentum of the leading jet p^*_{T1} provides a threshold for the cross section factorization validity hence the factorization scale is chosen to be $\mu^2 = p^{*2}_{T1} + Q^2$.

The scattering angle of particles θ, measured with respect to the positive z-axis, is not invariant under the Lorentz boost along the z-axis. The boost invariant rapidity y is introduced:

$$y = \frac{1}{2} \ln \frac{E + p_z}{E - p_z} \qquad (2.41)$$

In the limit of high energy, $E \approx |p|$, the rapidity y is approximated by

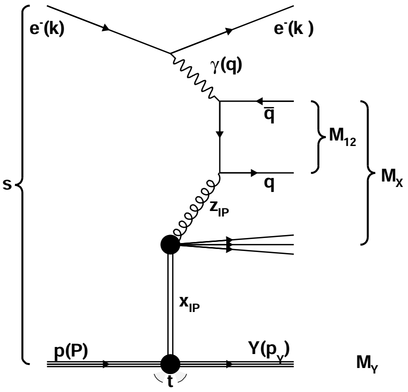

Figure 2.8: Schematic diagram of diffractive dijet production.

pseudorapidity η:

$$\eta = -\ln\left(\tan\frac{\theta}{2}\right) \tag{2.42}$$

Jet Algorithm

A jet algorithm or a jet finder refers to a procedure of clustering objects, so called protojets, into collimated sprays of particles, jets. The protojets can be partons, hadrons or jets stemming from intermediate steps of the jet finding. The jet cross section calculated in pQCD must be infrared and collinear safe [22]. Jet finders that meet these requirements combine the protojets based on distance measures

$$d_{ij} = \min(k_{Ti}^{2p}, k_{Tj}^{2p})\frac{\Delta_{ij}^2}{R^2} \tag{2.43}$$

$$d_i = k_{Ti}^{2p} \tag{2.44}$$

where k_{Ti} denotes the transverse momentum of a protojet i and $\Delta_{ij}^2 = (\phi_i - \phi_j)^2 + (\eta_i - \eta_j)^2$ with ϕ_i and η_i being the azimuthal angle and pseudorapidity of the protojet i respectively. The parameter p relates the geometrical distance Δ_{ij} to the distance in the transverse momenta of the protojets. The choice $p = 1$ corresponds to the longitudinally invariant k_T-algorithm [22, 23], $p = 0$ is used within the Cambridge/Aachen algorithm [24] and $p = -1$ corresponds to the anti-k_T algorithm [25]. The parameter R is related to a different class of jet algorithms which make use of momentum flow within a cone of radius R [26]. The k_T-algorithm with $R = 1$ is used in this analysis. The clustering is performed iteratively, each iteration proceeds in three steps

- The distance d_{ij} is evaluated for each pair of protojets, as well as the beam distance d_i for each protojet.
- The minimum d_{min} among all d_{ij} and d_i is found. If $d_{min} = d_i$ the protojet i is concerned as a jet and does not entry the algorithm anymore. If $d_{min} = d_{ij}$ the protojets i, j are combined in a single protojet.
- The first step is repeated until there are no protojets left.

The combination of two protojets can be defined in several manners, the p_T-recombination scheme [27] is used in this analysis.

2.4 Monte Carlo Generators

Monte Carlo (MC) generators are programs producing high energy physics events. They allow to generate a variety of final states given the initial configuration of beam particles. A MC generator implements a certain physics model and the final states production proceeds according to relevant matrix elements.

DIS events production, both inclusive and diffractive, is implemented in the RAPGAP MC program [28]. RAPGAP generates the DIS events based on the LO hard scattering matrix elements which include both BGF and QCD Compton (QCDC) processes mediated by either the γ or Z^0 exchange. The parton showers are treated according to the DGLAP equations. The hadronization is implemented in the same way as in the PYTHIA generator [29], e.g. the Lund string fragmentation model is used. The HERACLES program [30] is interfaced within RAPGAP and provides the simulation of the initial and final state QED radiation as well as the vacuum polarization and virtual corrections to the lepton vertex.

2.5 NLO Calculations

The NLO calculations used in this work make use of the Catani-Seymour dipole subtraction method [31]. This method is implemented in the nlojet++ program, which is a c++ program providing LO and NLO calculations of the multi-jet production cross section [32].

The nlojet++ is accommodated for the calculation of the diffractive cross section. The electron-proton scattering is effectively replaced with the electron-pomeron scattering by the downscale of the proton energy by factor $x_{I\!P}$. The calculations are performed for central values of intervals $(x_{I\!P}, x_{I\!P} + dx_{I\!P})$ and the total cross section is than obtained by integrating over the desired $x_{I\!P}$ range. The cross section for every $x_{I\!P}$ interval is weighted by the relevant pomeron flux and the pomeron parton densities are taken instead of the proton PDFs. This method relays on the Regge factorization as well as the QCD theoretical conclusions.

Chapter 3

HERA and H1 Detector

3.1 HERA Accelerator

The Hadron Elektron Ring Anlage (HERA) [33] is an electron-proton collider located at Deutsches Elektronen Synchrotron (DESY) laboratories in Hamburg. The accelerator operated in years 1992-2007 and delivered the integrated luminosity of ~ 500 pb^{-1} to each of the two major experiments H1 and ZEUS.

A tunnel situated from 10 to 20 m beneath the surface houses the main storage rings for protons and electrons. The rings consist of four straight sections, each 360 m long, and four circular sections of radius 790 m. The total main circuit accelerating path reaches about 6.3 km. The proton beam-pipe is equipped with high performance superconducting magnets ($B \sim 4.5$ T) operating at temperature of 4.2 K while the electron beam-pipe makes use of ordinary magnets. Besides the two collider experiments H1 and ZEUS the HERA collider also provides the high energy beams for the two fixed target experiments HERA-B and HERMES. The schematic view of the accelerator facilities is shown in Figure 3.1.

The main ring injection energies for protons (40 GeV) and electrons (14 GeV) are reached in a smaller storage ring called Positron Elektron Ring Anlage (PETRA). PETRA ring is pre-staged with a system of smaller storage rings, linear accelerators and synchrotrons.

The final energy of the proton and electron beam is 920 and 27.6 GeV respectively, which provides the total center of mass energy of ~ 320 GeV. The main ring stores about 220 bunches of particles. Each bunch contains $\sim 10^{11}$ particles obeying Gaussian density distribution with $\sigma = 11$ cm. The distance between individual bunches is 28.8 m resulting in 10.4 MHz bunch

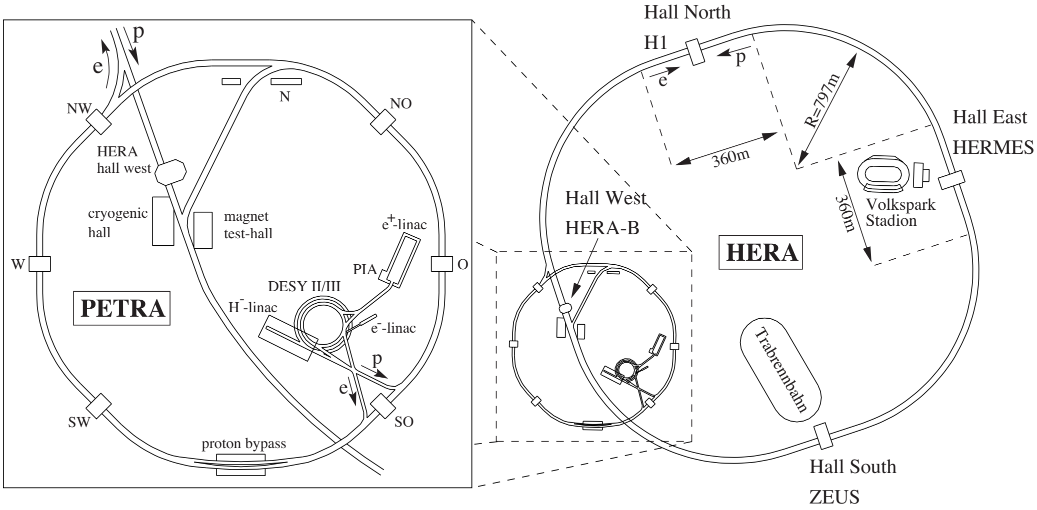

Figure 3.1: Schematic view of the HERA storage rings and the adjacent accelerating facilities. Locations of the two collider experiments H1 and ZEUS as well as the fixed target experiments HERMES and HERA-B are sketched.

crossing rate.

In years 1992-2000, during so called HERA-I running period, the proton beam energy was 820 GeV and the total integrated luminosity reached 140 pb^{-1}. The HERA-II running period refers to the data taking in years 2003-2007 when the collider was operated with the 920 GeV proton beam and the higher luminosity was achieved by the stronger beam focusing. During the HERA-II period the total integrated luminosity of almost 400 pb^{-1} was collected.

3.2 H1 Detector

H1 detector is a large acceptance particle detector located in the experimental hall North. Various subdetectors mostly arranged in cylindrical layers around the beam pipe cover the most of the solid angle around the nominal interaction point. The laboratory reference frame is chosen to be a right handed coordinate system with the origin at the interaction point, the $+z$ direction defined along the proton beam direction and the $+x$ direction pointing towards the center of the HERA ring. It is common to use a spherical coordinate system (r, θ, ϕ) where $\theta = 0$ and $\theta = \pi$ corresponds to the proton (forward) and electron (backward) direction respectively. The forward region of the H1 detector deals with high multiplicity states due to the higher energy of the proton beam and therefore is massively segmented. The backward region is designed for the scattered electron detection. A schematic drawing of the H1 detector and its main subdetectors is shown in Figure 3.2.

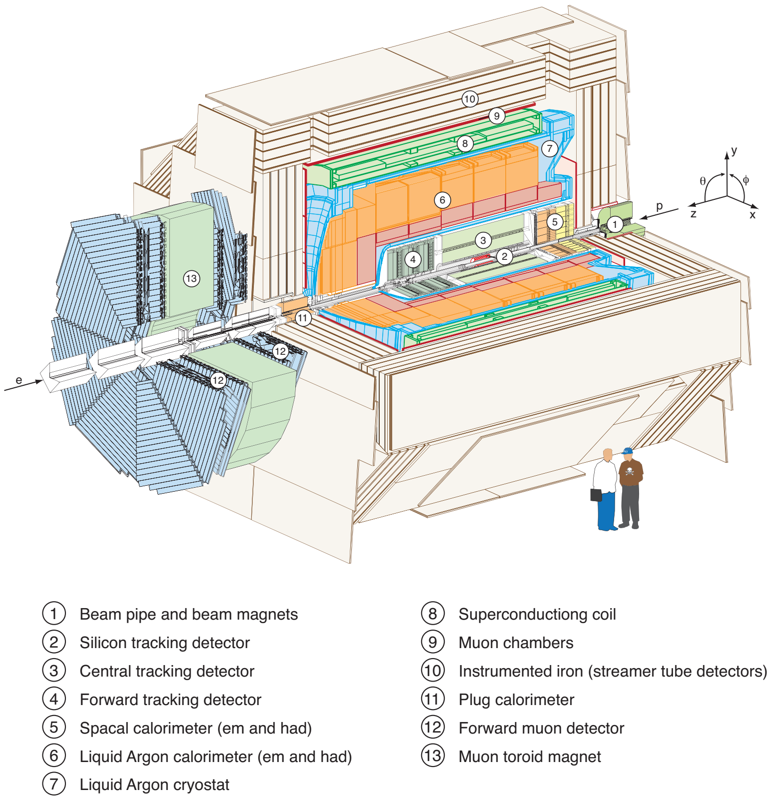

Figure 3.2: Schematic view of the H1 detector and its main subdetectors.

Detailed technical information on the H1 experiment can be found in [34, 35]. The components of the H1 detector that are directly involved in this analysis are briefly described in the following.

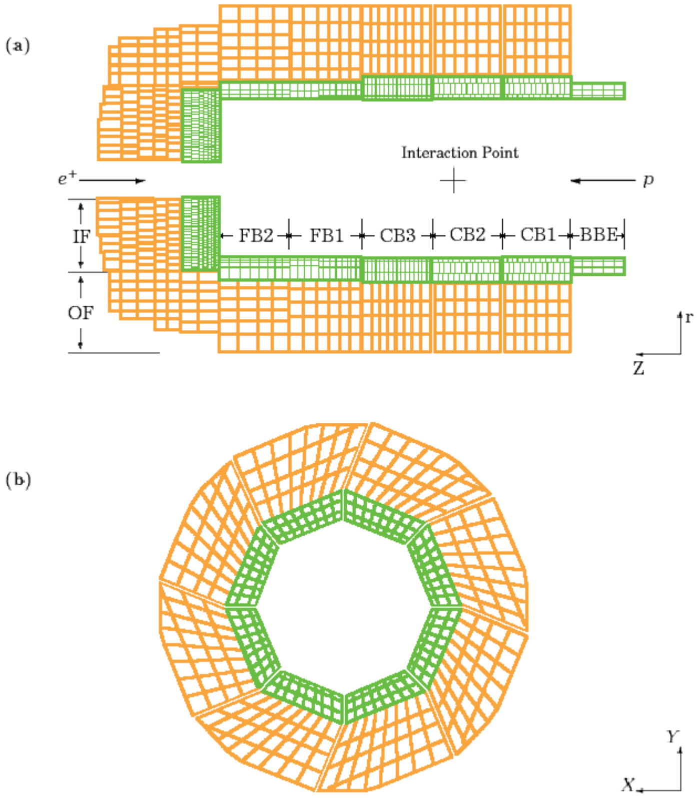

Figure 3.3: The side view of the LAr calorimeter (a) and the radial view of a single wheel (b). The electromagnetic and hadronic sections are displayed in green and orange color respectively.

3.2.1 Calorimetry

Liquid Argon Calorimeter

The Liquid Argon Calorimeter (LAr) is a high granularity non-compensating calorimeter covering the the polar angle of $3.8° < \theta < 155°$. Overall 44000 cells are situated inside a cryostat vessel filled with the active medium, the liquid argon. The LAr calorimeter is segmented into eight wheels (octants) along the z-axis. The inner (outer) layers of the wheels serve as the electromagnetic (hadronic) part of the calorimeter (see Figure 3.3). The electromagnetic part is equipped with 2.3 mm thick lead absorbers and its total size corresponds to 20-30 radiation lengths while the hadronic part is equipped with 16 mm stainless steel absorbers reaching 5-8 interaction lengths. The energy resolution is $\sigma_{em}(E)/E = 0.12/\sqrt{E[\mathrm{GeV}]} \oplus 0.01$ for electromagnetic showers and $\sigma_{had}(E)/E = 0.50/\sqrt{E[\mathrm{GeV}]} \oplus 0.02$ for hadronic showers. The response to a hadronic shower is reduced by 30% compared to an electromagnetic shower of the same energy and the hadronic energy is accommodated within the offline reconstruction. The LAr calorimeter allows to detect high energy jets, electrons and muons, as well as neutral particles.

Backward Lead Scintillator Calorimeter

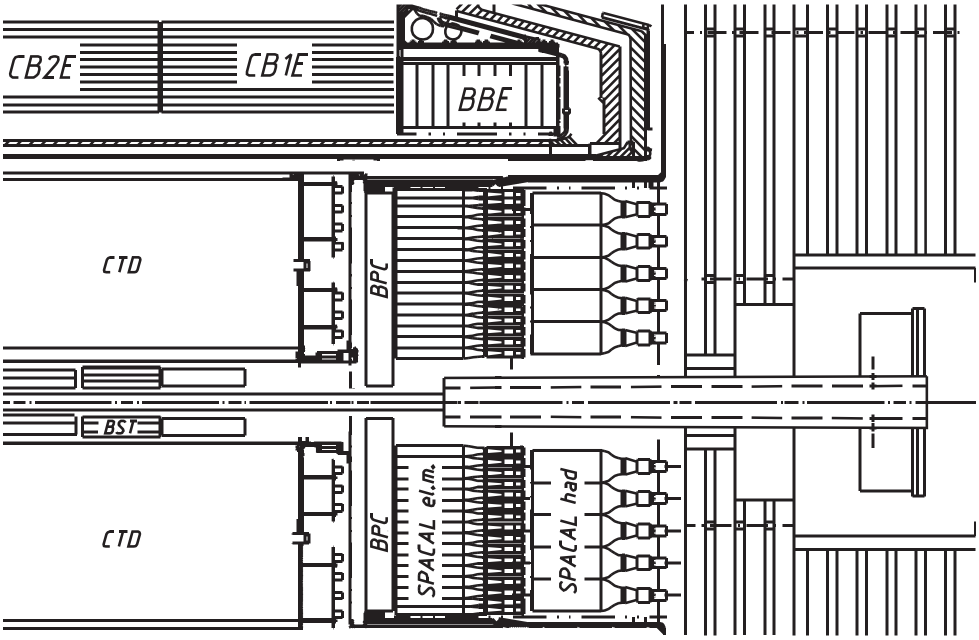

Figure 3.4: Side view of the backward part of the H1 detector.

The backward lead scintillator calorimeter, mostly referred to as 'spaghetti' calorimeter (SPACAL), covers the backward region $153^\circ < \theta < 173^\circ$. The location of SPACAL within the H1 detector is depicted in Figure 3.4. SPACAL is a non-compensating calorimeter consisting of electromagnetic and hadronic part, both equipped with lead absorbers and bunches of scintillation fibers (see Figure 3.5). SPACAL is designed for the high precision measurement of the scattered electron in DIS. The electromagnetic part corresponds to 28 radiation lengths while the hadronic part corresponds to 1 interaction length only. Both parts reach 2.2 interaction lengths in total and SPACAL is thus not feasible to detect jets. The energy resolution

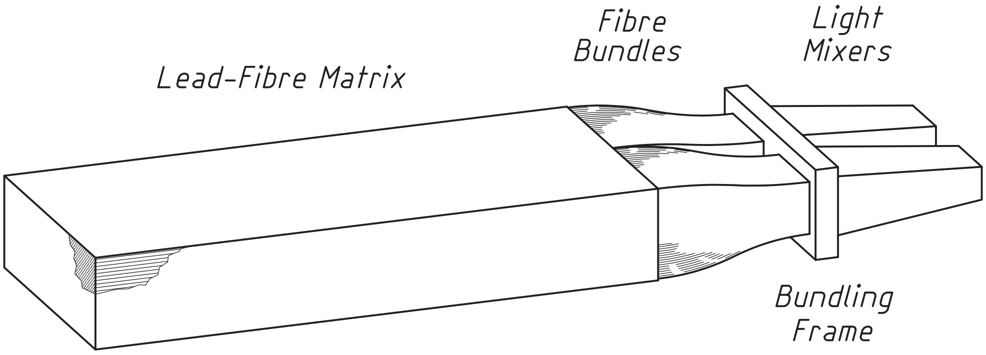

Figure 3.5: Sketch of a single SPACAL module.

is $\sigma_{em}(E)/E = 0.07/\sqrt{E[\mathrm{GeV}]} \oplus 0.01$ for the electromagnetic section and $\sigma_{had}(E)/E = 0.50/\sqrt{E[\mathrm{GeV}]} \oplus 0.02$ for the hadronic section.

PLUG Calorimeter

The PLUG calorimeter covers the forward region within $0.6^\circ < \theta < 3.5^\circ$ enlarging thus the acceptance of the LAr calorimeter down to the beam-pipe. The absorber material is copper arranged in nine plates along the beam-pipe. The resolution of the PLUG calorimeter is $\sigma_{had}(E)/E = 1.50/\sqrt{E[\mathrm{GeV}]}$.

3.2.2 Tracking

The H1 tracking system is divided into the Central Track Detector (CTD) and the Forward Track Detector (FTD). The longitudinal view of the H1 tracking system is depicted in Figure 3.6.

Central Track Detector

CTD comprises drift and proportional chambers as well as silicon trackers. The radial cross section of the CTD is sketched in Figure 3.7.

Two massive Central Jet Chambers (CJC1, CJC2) cover the scattering angle in range of $15^\circ < \theta < 165^\circ$. The both chambers consist of anode wires stretched parallel to the beam pipe, while the drift cells are ordered within 30° in the radial direction. This configuration ensures that the ionization electrons drift perpendicularly to the radial direction due to the presence of the 1.15 T magnetic field. The single hit resolution in the $r\phi$ plane is

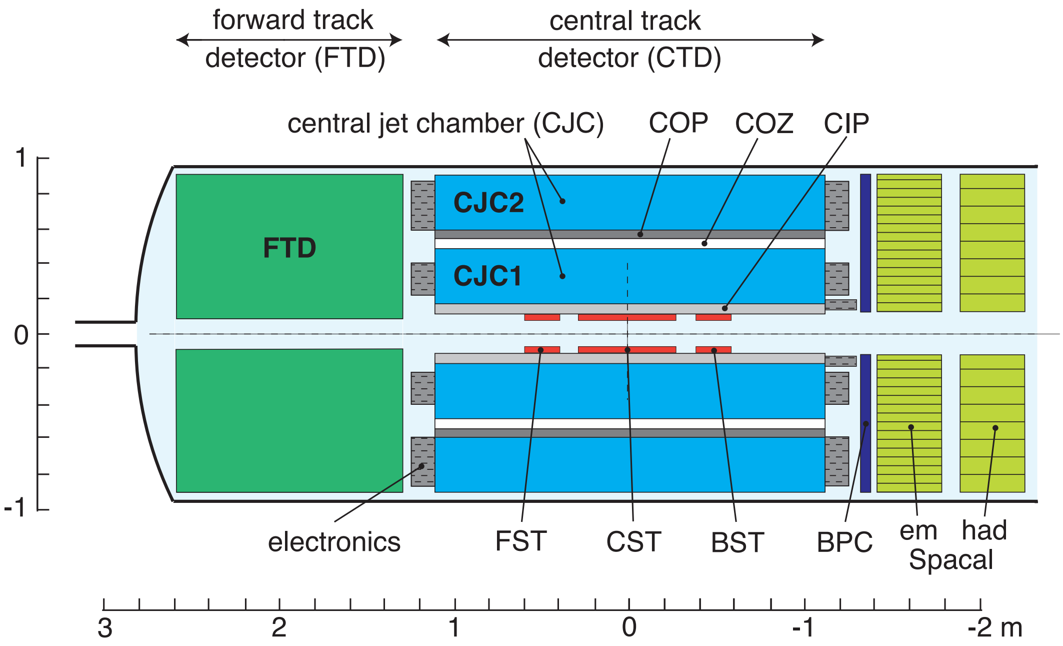

Figure 3.6: Side view of the H1 tracking system.

$\sigma_{r\phi} \sim 170\ \mu$m while the z coordinate is measured with the resolution of $\sigma_z \sim 2.2$ cm.

The z resolution is further improved by the Central Inner and Outer (CIZ and COZ) drift chambers. The CIZ resp. COZ are mounted on the inner resp. outer side of CJC1. The CJCs are supplemented with two thin Multiwire Proportional Chambers (MWPC), the Central Inner and Outer Proportional Chamber (CIP and COP). Both CIP and COP provide the information for the first trigger level (see section 3.2.4) since their response time is shorter than the time between the successive bunch collisions.

The momentum resolution of $\sigma(p)/p^2 < 0.01$ GeV^{-1} is achieved due to the combined information of CJCs, CIZ and COZ.

The tracking system relays further on three silicon trackers, the Forward, Central and Backward Silicon Trackers (FST, CST and BST). CST surrounds the nominal interaction point and is mounted at distance of 5 cm from the beam-pipe. The aim of CST is to provide precise vertex information including secondary vertexes from heavy flavor decays. CST single hit resolution is 12 μm in the $r\phi$ plane and 22 μm in the z-direction. The CST angular coverage is $30° < \theta < 150°$. BST extends this coverage to

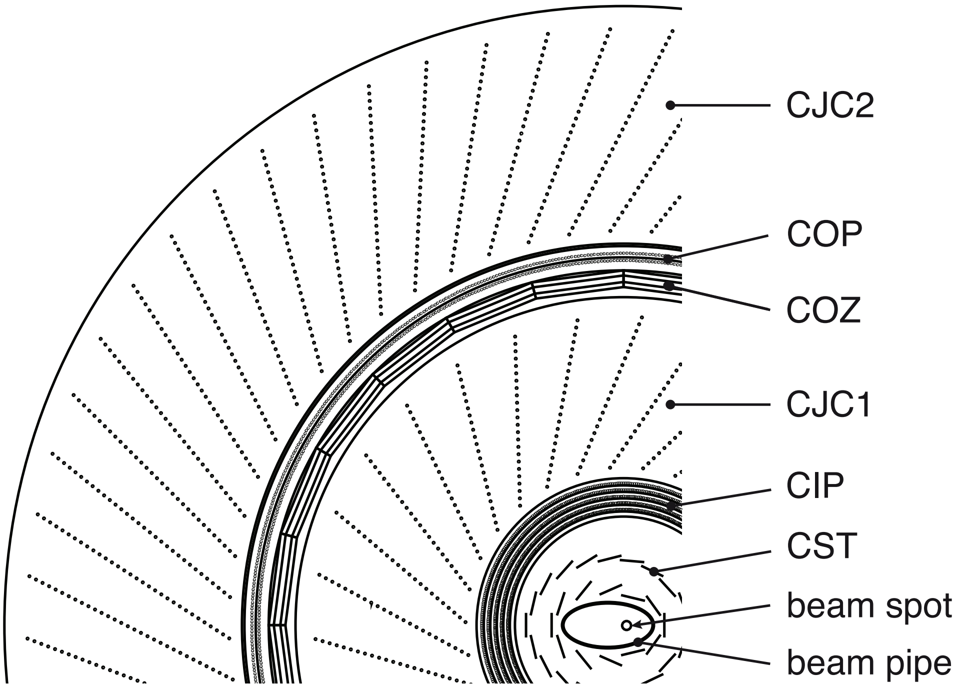

Figure 3.7: Front view of the H1 tracking system.

$165^\circ < \theta < 176^\circ$ and serves mainly to improve the scattered electron identification while FST covers the forward region with $7^\circ < \theta < 19^\circ$.

Forward Track Detector

The Forward Track Detector (FTD) extends the geometric acceptance of the tracking system to $5^\circ < \theta < 25^\circ$. FTD consist of three modules each comprising planar and radial drift chambers. The typical FTD momentum resolution is $\sigma(p)/p^2 \sim 0.1$ GeV^{-1}.

3.2.3 Forward Detectors

Forward Muon Detector

The Forward Muon Detector (FMD) consists of six double layered drift chambers and a toroidal magnet (see Figure 3.8). Two chambers are designed to measure the azimuthal angle ϕ and the remaining four to measure

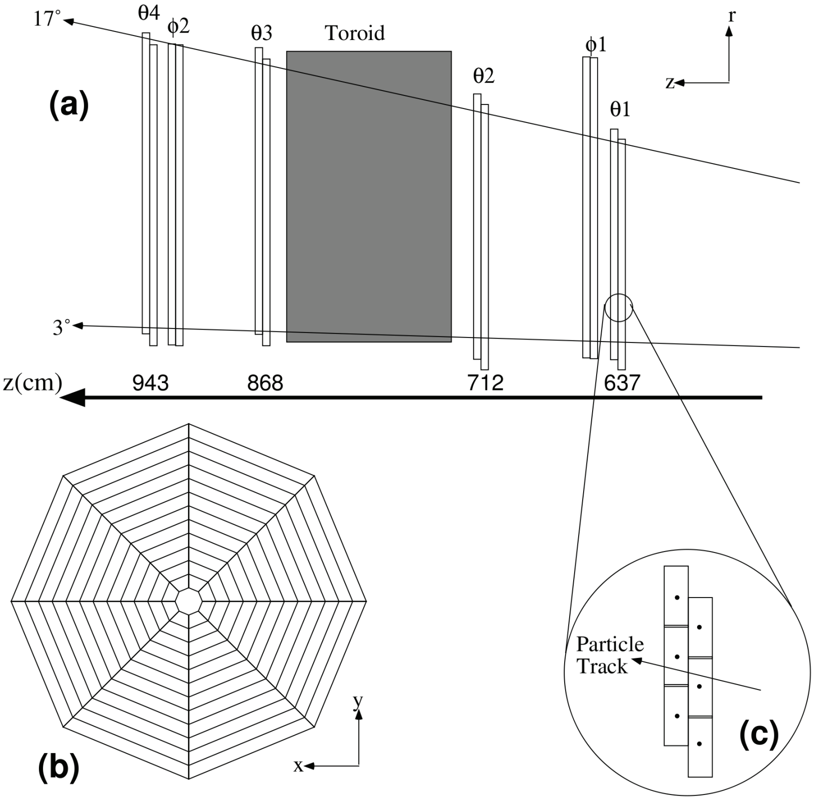

Figure 3.8: Side view of the forward muon detector (a). Front view of a single octagonal layer (b). A hit pair produced in a double-layer (c).

the polar angle θ with the acceptance in range $3^\circ < \theta < 18^\circ$. Due to the presence of the toroidal magnet, FMD is feasible for momentum reconstruction from 5 to 500 GeV.

Forward Tagger System

The Forward Tagger System (FTS) is designed to detect particles stemming from the proton remnant. FTS consist of four scintillator layers mounted at 26, 28, 53 and 92 m distance from the nominal interaction point. Individual layers surround the beampipe and comprise four counters each. There is one scintillator per counter for 26 and 28 m layers, while the counters for layers at 53 and 92 m consist of two scintillators.

3.2.4 Trigger System

Although the bunch crossing rate at HERA reaches 10.4 MHz, not every collision produces an event of physics interest. The H1 trigger system is designed to distinguish between signals originating from the *ep* interaction and the detector activity caused by events classified as the background. The main background sources are synchrotron radiation of the electron beam, stray protons hitting surrounding materials, protons interacting with the beam-pipe gas, beam halo muons and cosmic ray muons. The trigger decision is done subsequently at four stages. The architecture of the H1 trigger system is schematically depicted in Figure 3.9.

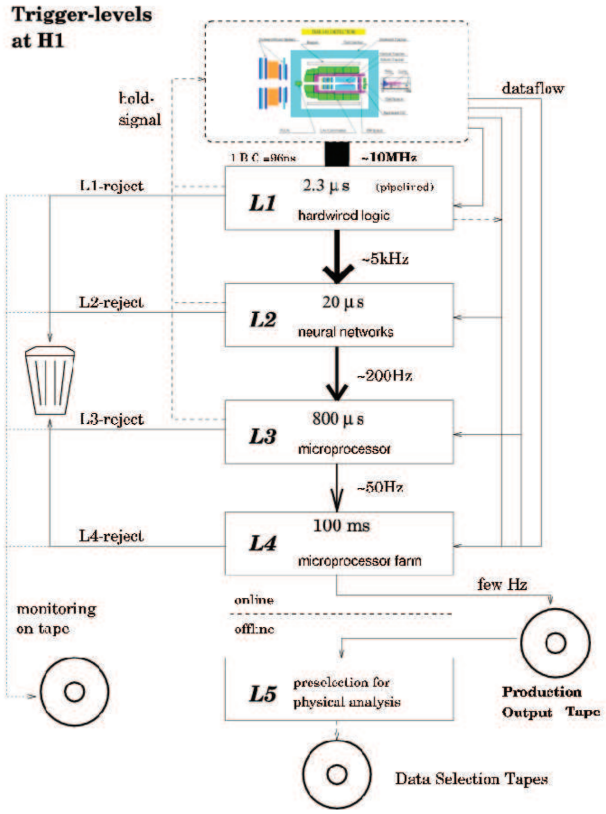

Figure 3.9: Schematic drawing of the H1 trigger system.

The trigger level one (L1) collects information from nine trigger systems that correspond to particular subdetectors. Information from a set of 256 trigger elements (TE) is buffered in pipelines synchronously to HERA clock at frequency of 10.4 MHz. The L1 latency time of ~ 2 μs constrains the minimum pipeline length which ensures that every bunch crossing is subjected to the L1 decision. The TE are read by Central Trigger Logic (CTL) where they are combined into 128 subtriggers. Most subtriggers are dedicated to particular physics processes while some of them serve for monitoring of individual subdetectors and physics triggers. The CTL decides to keep an event if at least one subtrigger condition is fulfilled. If the event is rejected the pipelines are overwritten without imposing the dead time. If the event is accepted the readout is stopped and and the event is submitted to higher trigger levels. The original bunch crossing rate is scaled down to ~ 1 kHz at this trigger stage.

The second trigger level (L2) depends on the information delivered by the L1 and relays on two independent trigger systems, the neural network (L2NN) and the topological trigger (L2TT). L2NN [36] consists of 13 neural networks working in parallel and was introduced to improve the trigger system performance after the luminosity upgrade. L2TT incorporates up to 16 trigger elements that combine topological information from various subdetectors. The L2 decision is available within 20 μs.

The third trigger level (L3) decision is based on the Fast Track Trigger (FTT) [37, 38]. This trigger system is capable to reconstruct decays of particle resonances making use of the L2 tracks. The L3 system involves a farm of commercial processors with a real time operating system. The L3 latency time is about 100 μs.

At the last trigger level (L4), the final decision whether to keep or downscale the event is done. Events that passed the lower level triggers are checked again with higher precision, which results in further event reduction by ~ 50 %. The L4 trigger is not synchronized with the HERA clock and the calculations are performed by means of an independent processor farm. The events are recorded for offline analyses to a Data Summary Tape (DST) with a frequency of few Hz.

3.2.5 Luminosity System

Measurement of luminosity at HERA makes use of the Bethe-Heitler process $ep \to ep\gamma$, for which the cross section σ is calculable in QED. The integrated luminosity $L = \int \mathcal{L} dt$ is determined from the number of events N

$$N = \sigma L \tag{3.1}$$

The instantaneous luminosity $\mathcal{L}$ is given by the measured event rate of the Bethe-Heitler process. The H1 luminosity system consists of two detectors

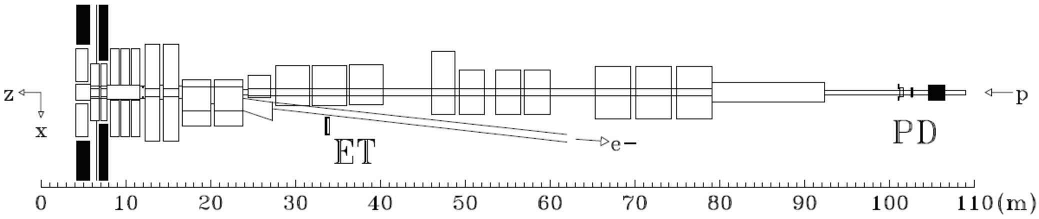

Figure 3.10: The H1 luminosity system.

mounted close to the beam-pipe in sufficient distance from the interaction point. Outgoing electrons are tagged by an Electron Tagger (ET) at $z = -40$ m while photons are measured in an Photon Detector (PD) at $z = -102$ m. The scheme of the luminosity system is depicted in Figure 3.10.

3.2.6 Detector Simulation

The H1 detector response is simulated by means of dedicated software, H1SIM, which is based on GEANT3 [39] algorithm. H1SIM implements the detector geometry, particle interactions with the material as well as tracking. Test beam measurements with detector prototypes together with instant monitoring of the full detector response provide the verification and further tuning of the simulation. The output of the H1SIM has the same form as the real *ep* data and both MC and data events are reconstructed by the same program, H1REC.

Chapter 4

Data and Monte Carlo

4.1 Analyzed Data

The measurement of the dijet cross section in NC DDIS presented in this work makes use of the data collected during the HERA II period. The data taking at H1 was realized in time intervals with stable experimental conditions called runs. A run can be classified either as good, medium or poor based on the overall detector performance, background and beam conditions. Only good and medium runs with the minimum luminosity of 0.2 pb^{-1} are analyzed in this measurement. The quality of a run is further ensured by demanding specific sub-detectors to be in operation and fully read out. Only runs where the LAr calorimeter, CJCs, CIP, ToF and luminosity system are operational are accepted. The luminosity is recorded per each run and is corrected offline since the information from the luminosity system is not immediately available during the data taking. The total integrated luminosity of 281pb^{-1} of the analyzed sample corresponds to the sum of luminosities of individual selected runs. The run range and luminosity for data collected in years 2006-2007 are summarized in Table 4.1

4.2 Monte Carlo

A set of MC samples with underlying processes expected in data is produced in desired phase space. MC is utilized to translate the measured event rate into the cross section at level of stable hadrons and for statistical subtraction of a background. Another set is produced without the detector simulation and is used to quantify the QED radiation and hadronization effects.

Period	Lepton	Run range	$L[\mathrm{pb}^{-1}]$
2005	e^-	401617-436893	104.58
2006	e^-	444307-466997	51.57
2006	e^+	468531-492541	81.87
2007	e^+	492559-500611	45.69
HERA 2		401617-500611	283.71

Table 4.1: Overview of the selected run periods and the total integrated luminosities.

4.2.1 Overview of MC Samples

The Signal MC sample is generated with the RAPGAP31 program. The NC DDIS events are produced according to relevant QCD matrix elements calculated to the first order of the perturbation expansion. The contribution from higher orders are modeled by means of hadronic showers. The particular model used by RAPGAP refers to Leading Logarithm Parton Shower (LLPS) approach []. As a DPDF input for the MC calculations, values given by the H1 2006 Fit B [] are used. The Lund string model is employed to describe the fragmentation of partons into detectable hadrons. Both BGF and QCDC processes realized via the pomeron exchange are generated with either light quarks or charm in the final state. The Reggeon exchange is only considered with light quarks in the final state, since the charm contribution is not discernible at the $x_{\mathbb{P}}$ range of interest.

The contribution of events with the scattered proton found in low mass dissociation state is included in the signal MC as well. The set of dissociative samples is produced with RAPGAP in the same manner as for the elastic scattering. Possible dissociative Reggeon contribution is neglected.

In low Q^2, resolved pomeron processes may play role. Additional signal MC sample is produced with RAPGAP utilizing the resolved pomeron model.

Each of the discussed MC samples is generated in three distinct sets corresponding to run periods of the data taking and to the appropriate lepton type. The electron samples are submitted to the detector simulation separately for periods 2005 and 2006 while the positron samples are simulated for the period 2006/2007.

The main source of background events is the non-diffractive DIS jet production. A fraction of events with a measured rapidity gap in HFS may still stem from inclusive processes. Additionally, the effectivity of detecting diffractive events based on rapidity gap identification is limited. A RAP-

Purpose	Process	Events	Luminosity [pb^{-1}]
Signal	uds, pomeron	5×10^6	4177.5
Signal	charm, pomeron	5×10^6	6127.7
Signal	light quarks, reggeon	5×10^6	17610.0
Signal	uds, pomeron, prot. dissociation	5×10^6	4603.5
Signal	charm, pomeron, prot. dissociation	5×10^6	6114.8
Signal	resolved pomeron	5×10^6	4177.5
Background	DIS jet production	1×10^7	212.5

Table 4.2: Overview of MC samples.

GAP31 MC sample simulating inclusive DIS jet production is taken into account as a background contribution.

The QED radiation corrections are determined based on a radiative and non-radiative RAPGAP samples that are generated under the same conditions as the signal sample but with larger statistics. The hadronization corrections are determined making use of samples without QED radiation that differ in modeling of parton showers. Another set utilizing Color Dipole Model (CDM) of parton showers is used in course of the hadronization effects evaluation.

An overview of the MC samples that model the signal and background contributions is shown in Table 4.2.

4.2.2 Detector, Hadron and Parton Level

Calculation of kinematic variables can be performed at three different stages for a set of MC events which passed the detector simulation.

- Detector level refers to the kinematic reconstruction based on directly detected objects (tracks, energy clusters). Assuming a proper detector simulation, the relevant variable calculation and event selection criteria can be uniquely applied in both data and MC. Kinematic distributions at the detector level of MC are thus directly comparable to the distributions measured in data.

- Hadron level refers to kinematic variables defined in terms of stable hadrons which emerge as products of hadronization.

- Parton level refers to kinematic variables evaluated based on four-momenta of partons, leptons and intermediate bosons that take part in the hard scattering. Quantities calculated at the parton level and their relation to the hadron level serve for investigation of hadronization effects.

4.3 Reconstruction of Kinematics

The kinematic variables introduced in Chapter 2 are reconstructed based on the measurement of the scattered electron and the Hadronic Final State (HFS). The DIS kinematics reconstruction makes use of the electron-Σ method [40], which provides an accurate resolution of the kinematic variables in the desired kinematic range of DIS processes [41]. The squared momentum transfer Q^2 is calculated from the scattered electron information in the e-Σ method:

$$Q_e^2 = E_e E_e'(1 + \cos\theta_e) \tag{4.1}$$

where $E_e \approx 27.6$ GeV is the energy of the beam electron while E_e' and θ_e denote the energy and polar angle of the scattered electron. The reconstruction of the inelasticity y includes the information from the HFS measurement through a variable y_h defined as

$$y_h = \frac{\sum_i (E_i - p_{z,i})}{2E_e} \tag{4.2}$$

The summation runs over all HFS objects with energy E_i and momentum component $P_{z,i}$. Within the e-Σ method, the y is reconstructed in the following way:

$$y_{e\Sigma} = \frac{Q_e^2}{x_\Sigma s} \tag{4.3}$$

$$x_\Sigma = \frac{Q_\Sigma^2}{y_\Sigma \cdot s} \tag{4.4}$$

$$Q_\Sigma^2 = \frac{E_e^2 \cdot \sin^2\theta_e}{1 - y_\Sigma} \tag{4.5}$$

$$y_\Sigma = \frac{2y_h \cdot E_e'}{2y_h \cdot E_e' + E_e \cdot (1 - \cos\theta_e)} \tag{4.6}$$

where s denotes the center of mass energy of the electron-proton system. The photon-proton center of mass energy W^2 is reconstructed as

$$W^2 = y \cdot s - Q^2 \tag{4.7}$$

The longitudinal fraction of the proton momentum carried by the pomeron is evaluated using the invariant mass M_X of the system X

$$x_{I\!P} = \frac{Q^2 + M_X^2}{Q^2 + W^2} \tag{4.8}$$

$$M_X^2 = f(\eta_{max}) \sum_i P_i^2 \tag{4.9}$$

where the sum counts fourmomenta P_i of all HFS objects and $f(\eta_{max})$ is a factor depending from LAr cluster rapidity and is introduced in order to improve the detector resolution. At the hadron level, the defining relation 2.34 is used for the calculation of $x_{I\!P}$, since the relevant fourmomenta are known based on the MC generator information. The fraction of the pomeron momentum carried by the parton entering the hard scattering is reconstructed by means of the invariant mass of the two jets M_{12} as

$$z_{I\!P} = \frac{Q^2 + M_{12}^2}{Q^2 + M_X^2} \tag{4.10}$$

The energy carried by the jet system relative to the total energy of HFS is reconstructed as follows:

$$x_\gamma = \frac{\sum_{jet}(E_i^* - P_{z,i}^*)}{\sum_{HFS}(E_i^* - P_{z,i}^*)} \tag{4.11}$$

The above formula holds exclusively in the γ^*-proton rest frame in case of DIS.

Correspondence between the level of stable hadrons and detector level is discussed in Section 4.6.

4.4 Event Selection

4.4.1 NC DIS Selection

Trigger Selection

The online triggering of events containing the scattered electron is performed by means of the subtrigger S61. The S61 decision is accomplished making use of information from SPACAL and CJC. The energy deposit in SPACAL of at least 9 GeV is required together with at least one CJC track with a minimum transverse momentum of 900 MeV. The track condition is validated by means of FTT. S61 accepts the events at level L4 with a prescale of ~ 1, which is valid in the range of the photon virtuality under investigation.

Vertex Requirement

The precise information on the ep interaction position is of vital importance for a proper event kinematics reconstruction. The direction of the scattered electron is required to be reconstructed with respect to the actual vertex position. The coordinates of the interaction vertex are determined with the track chambers CJC1 and CJC2. Although the designed interaction point lays in the center of the detector, the real vertex position is Gaussian-smeared around $z = 0$ with $\sigma \sim 10$ cm. A cut of $|z_{vtx}| < 35$ cm ensures the event originates from the ep interaction.

Electron Identification

The scattered electron is reconstructed based on the information from the SPACAL calorimeter. The radial and azimuthal angle of the scattered electron θ_e and ϕ_e are reconstructed regarding the vertex position and the actual beam position. Given the measured position of the SPACAL cluster x_{clus}, y_{clus}, z_{clus} and the position of the interaction vertex x_{vtx}, y_{vtx}, z_{vtx}, the scattering angles of the electron are given by

$$\tan\theta = \frac{\sqrt{(x_{clus} - x_{vtx})^2 + (y_{clus} - y_{vtx})^2}}{z_{clus} - z_{vtx}} \tag{4.12}$$

$$\tan\phi = \frac{y_{clus} - y_{vtx}}{z_{clus} - z_{vtx}} \tag{4.13}$$

The scattering angles corrected for the actual position of the beam are reconstructed as

$$\cos\theta_e = s_x \sin\theta\cos\phi + s_y \sin\theta\sin\phi + s_z \cos\theta_e \tag{4.14}$$

$$\tan\phi_e = \frac{y_{vtx} - y_0 - y' z_{clus}}{x_{vtx} - x_0 - x' z_{clus}} \tag{4.15}$$

where x_0, y_0 denote the beam position at $z = 0$ while x', y' denote the beam direction in the xy plane. The coordinates of the beam direction vector $\vec{s}$ are given as

$$s_x = \frac{x'}{\sqrt{x'^2 + y'^2 + 1}}, s_y = \frac{y'}{\sqrt{x'^2 + y'^2 + 1}}, s_z = \frac{1}{\sqrt{x'^2 + y'^2 + 1}} \tag{4.16}$$

In order to ensure the whole cluster is contained in the SPACAL volume the distance of the cluster from the beam axis in the $r\phi$ plane r_{SPACAL}

is constrained to $18 < r_{SPACAL} < 74$ cm. The cluster-beam distance is evaluated at $z = -160$ cm as

$$r_{SPACAL} = \tan\theta_e(-160 - z_{vtx}) \tag{4.17}$$

Since hadrons can be often misidentified as electrons the fraction of the energy of the cluster deposited in the hadronic part of the calorimeter is constrained by $E_{had}/E_{tot} < 15\%$ where E_{tot} denotes the total energy of the cluster. A typical hadronic shower is broader than an electromagnetic one hence the probability of a hadron faking an electron is further reduced by a cut applied on the energy weighted radius of the cluster $r_{log} < 4$ cm. The information from the individual cells contained in the cluster is accounted for in the following way:

$$r_{log} = \frac{\sum_i d_r \max(0,\ 4.8 + \log\frac{E_i}{E_{clus}})}{\sum_i \max(0,\ 4.8 + \log\frac{E_i}{E_{clus}})} \tag{4.18}$$

The sum runs over all cells within the cluster and d_r denotes the radial distance between the position of a cell (x_i, y_i) and the cluster barycentre

$$d_r = \sqrt{(x_i - x_{bar})^2 + y_i - y_{bar})^2} \tag{4.19}$$

The barycentre x_{bar} is introduced as

$$x_{bar} = \frac{\sum_i x_i \max(0,\ 4.8 + \log\frac{E_i}{E_{clus}})}{\sum_i \max(0,\ 4.8 + \log\frac{E_i}{E_{clus}})} \tag{4.20}$$

and y_{bary} is defined analogously. Electrons that belong to jets can also be misidentified as the scattered electron. Therefore energy deposited in a cone of radius $R^2 = (\Delta\eta)^2 + (\Delta\phi)^2$ in the $\eta\phi$ space is considered. The electron is isolated by requiring $E_{cone}/E_{tot} < 5\%$ where E_{cone} denotes the energy deposited in the hadronic section of the calorimeter within the cone. If there is more than one identified electron satisfying the above criteria the electron with the highest transverse momentum is accepted as the scattered electron. The electron selection cuts are summarized in Table 4.4. Details on the electron identification can be found in [].

Background Rejection

A fraction of the measured NC DIS signal originate in the QED Compton (QEDC) scattering ($ep \to ep\gamma$). A QEDC event is identified requiring at

Cut Value	Description
$N_{elmag} \geq 2$	Nr. of electromagnetic particles in SPACAL calorimeter
$E_1 > 4$ GeV	Energy of Candidates
$E_2 > 4$ GeV	
$E_1 + E_2 > 18$ GeV	
$-\cos(\phi_1 - \phi_2) > 0.95$	Acoplanarity

Table 4.3: Selection criteria for QED Compton scattering events.

Cut	Purpose
$\lvert z_{vtx} \rvert < 35$ cm	Interaction Vertex
$35 < E - p_z < 75$ GeV	DIS Energy and Momentum Conservation
$4 < Q^2 < 80$ GeV^2	DIS Phase Space
$0.1 < y < 0.7$	
$E_e > 9.5$ GeV	Electron Energy
$r_{log} < 4$ cm	Electromagnetic/Hadronic Cluster Separation
$E_{cone}/E_{tot} < 5\%$	
$18 < r_{SPACAL} < 74$ cm	SPACAL Acceptance
Anti-QEDC	Rejection of QED Compton Scattering

Table 4.4: NC DIS event selection criteria.

least two electromagnetic particles that are oriented in the opposite ϕ direction and correspond thus to the final state photon and electron. The selection criteria, based on which QEDC events are identified and rejected, are summarized in Table 4.3.

The photoproduction processes occur at very low scattering angles where the scattered electron typically escapes undetected. A HFS particle (e.g. pion) can leave energy deposit in SPACAL and mimic thus NC DIS event signal. Besides the cuts improving the accuracy of the electromagnetic and hadronic cluster separation (constrain on r_{log} and E_{had}/E_{tot}), the photoproduction background is further rejected making use of energy and momentum conservation. In a DIS event, the energy and longitudinal momentum is conserved according to $E - p_z = \sum_i (E_i - p_{z,i}) = 2E_e \sim 55$ GeV with the sum counting all HFS objects and the scattered electron. A restriction of $35 < E - p_z < 75$ GeV is required for the NC DIS selection.

4.4.2 Selection of DDIS Dijet Events

Diffractive Selection

The Large Rapidity Gap (LRG) selection of diffractive events relays on the presence of the characteristic gap in rapidities of the HFS objects that clearly separates the system X and Y. The most forward LAr cluster with energy above the noise threshold (800 MeV) is required to occur at a maximum rapidity of $\eta_{max} < 3.2$. Further, events causing activity in the forward region are refused based on the information from FMD, FTS and PLUG calorimeter.

FMD is sensitive to particles stemming from interactions of proton dissociation products with material of the beam pipe. The proton dissociation events are suppressed by demanding no activity in FMD. Only events with at most one hit pair in the first two layers and at most two hit pairs in the first three layers are accepted. The remaining three FMD layers located behind the toroid are not used in the selection due to higher noise.

The FTS located at $z = 28$ m is feasible to detect hadrons which originate in proton dissociation and occur at very high rapidity. In the LRG selection, events with no hits in FTS are accepted.

Energy measured in the PLUG calorimeter, that covers the region between LAr and FMD, is restricted by cut $E_{PLUG} < 3$ GeV ensuring thus there is no activity above the noise threshold.

Since the events at large $x_{I\!P}$ mostly originate in non-diffractive DIS processes the restriction of $x_{I\!P} < 0.03$ is required in addition.

The LRG selection cuts are summarized in Table 4.5.

Cut Value	Description
$\eta_{max} < 3.2$	Forward activity in LAr
$x_{I\!P} < 0.03$	Diffraction Phase Space
$N_{1+2}^{FMD} \leq 1$	Hit pairs in the first 2 FMD layers
$N_{1+2+3}^{FMD} \leq 2$	Hit pairs in the first 3 FMD layers
N_{28}^{FTS}	Hits in the FTS 28 m station
$E_{PLUG} < 3$ GeV	Energy in PLUG

Table 4.5: LRG selection cuts.

Jet Selection

Jets are reconstructed by means of the k_T algorithm in the photon-proton ($\gamma^* p$) center of mass system. The boost vector corresponding to the virtual photon is obtained from the reconstructed fourmomentum of the scattered electron. The boost transformation includes a rotation around the $\gamma^* p$ axis so that the scattered electron trajectory lays in the $z - x$ plane in the $\gamma^* p$ frame, i.e. $\phi_e^* = 0$. The leading and subleading jet transverse momenta have to fulfill $p_{T,1}^* > 5.5$ GeV and $p_{T,2}^* > 4.0$ GeV respectively. The asymmetric cut on the transverse momenta follows the assumptions necessary for the fixed order QCD prediction calculation. The geometric acceptance of the LAr calorimeter imposes restriction on the jet pseudorapidity in the laboratory frame $-1 < \eta_{1,2} < 2$. Events with at least two jets that meet the above criteria are selected. The criteria for selecting a dijet event are summarized in Table 4.6.

Cut Value	Description
$N_{jet} \geq 2$	Jet multiplicity
$p_{T,1}^* > 5.5$ GeV	Minimum transverse momentum in $\gamma^* p$
$p_{T,2}^* > 4.0$ GeV	
$-1.0 < \eta_{1.2} < 2.0$	Pseudorapidity in lab. frame

Table 4.6: Dijet selection cuts.

4.5 Trigger Efficiency

The trigger efficiency is determined based on the Analysis Sample (AS), which is selected by the investigated trigger, and the Reference Sample (RS), which is selected by triggers that are independent from the investigated trigger. Denoting $N(RS)$ the number of events in the reference sample and $N(AS \wedge RS)$ the number of events in both samples, the trigger efficiency is given by

$$\varepsilon_{Trig} = \frac{N(AS \wedge RS)}{N(RS)} \tag{4.21}$$

The trigger efficiency of S61 is studied separately for the SPACAL and FTT condition.

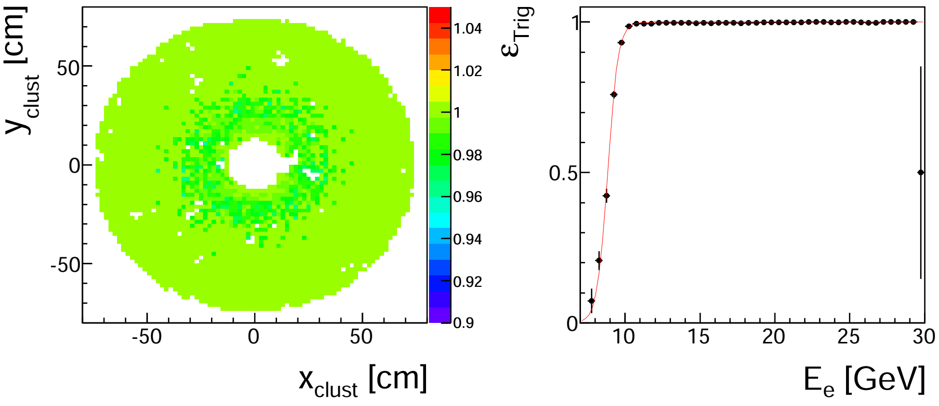

(a) (b)

Figure 4.1: S61 SPACAL condition trigger efficiency as a function of SPACAL cluster coordinates after the fiducial cuts (a) and the Fermi function fit (b). The data belong to the run period 2005e^-.

4.5.1 S61 SPACAL Trigger Efficiency

The inclusive DIS data sample, that serves as the analysis sample for the SPACAL S61 efficiency $\varepsilon^{Spac}_{Trig}$ determination, is selected by means of cuts defined in Table 4.4. The monitoring sample is selected within the same kinematic cuts but requiring any subtrigger independent from S61 to be set.

The SPACAL fiducial cuts defined in Table 4.4 are a priori unknown and are determined by a scan of the SPACAL S61 efficiency as a function of SPACAL cluster coordinates $\varepsilon^{Spac}_{Trig}(x, y)$. The regions of low trigger efficiency that correspond to improperly working SPACAL cells are excluded by requiring $\varepsilon^{Spac}_{Trig}(x, y) > 96\%$ (see Figure 4.1 (a)). Furthermore, the ϵ^{Spac}_{Trig} is expected to decrease with the energy of the scattered electron in the region $E_e < 11$ GeV. On the other hand, in order to ensure sufficiently large statistics for the measurement of the cross section up to $y < 0.7$, the cut on the scattered electron energy ought to be at least $E_e > 9.5$ GeV. The decrease in the trigger efficiency is described by the Fermi function

$$\varepsilon^{Spac}_{Trig}(E_e) = \frac{a}{\exp(b - E_e)/c + 1} \tag{4.22}$$

where a, b and c are parameters to be fitted. The inefficiency of the SPACAL part of S61 trigger is corrected for by reweighting the events in data by factor of $1/\varepsilon^{Spac}_{Trig}(E_e)$ obtained from the Fermi function fit to the trigger efficiency measured down to $E_e > 7.0$ GeV (see Figure 4.1). Figure 4.2 illustrates the trigger efficiency, where the analysis sample is corrected for by the Fermi function fit. The trigger efficiency remains above 99% after the correction for all analyzed run periods.

4.5.2 S61 FTT Trigger Efficiency

The correction of the measured event rate to the FTT S61 efficiency ϵ^{FTT}_{Trig} relays on the MC and is included in the unfolding of the cross section to the hadron level. The FTT trigger element should be therefore simulated in accordance with the efficiency observed in data. The MC analysis sample is selected by requiring the FTT trigger element to be set while the reference sample includes all events that passed the kinematics cuts. Both MC samples consist of a sum of the diffractive and non-diffractive sample normalized by factors derived in Section 4.7.1. The monitor subtrigger S0 is used for the run period $2005e^-$. The subtrigger S0 depends on the FTT condition for run periods $2006e^-$, $2006e^+$ and $2007e^+$, hence the subtrigger S1 is chosen as the monitoring trigger. The comparison of the data and MC FTT trigger efficiency for in Figure 4.3. The difference between the data trigger efficiency and the MC FTT emulation can be covered within 1/% which is propagated into the systematic error of the measurement.

4.6 Detector Effects in MC

The reconstruction efficiency and finite resolution of the detector put limitations on direct interpretation of the measured event rates as a cross section at the level of stable hadrons. The relevant correction of the measured spectra, often referred to as the unfolding of the data to the hadron level, is performed statistically by applying an appropriate correction factor to the each bin of the studied distribution. Besides a good description of the measured data by the MC simulation, this method is also sensitive to migrations between hadron and detector level quantities. A binning that leads to a meaningful differential cross section measurement has to be chosen regarding the hadron-detector resolution and correlation. The correlation and resolution, which is defined as R^{rec}/R^{gen} for an observable R, are studied within the full analysis cuts defined in Table 4.5.

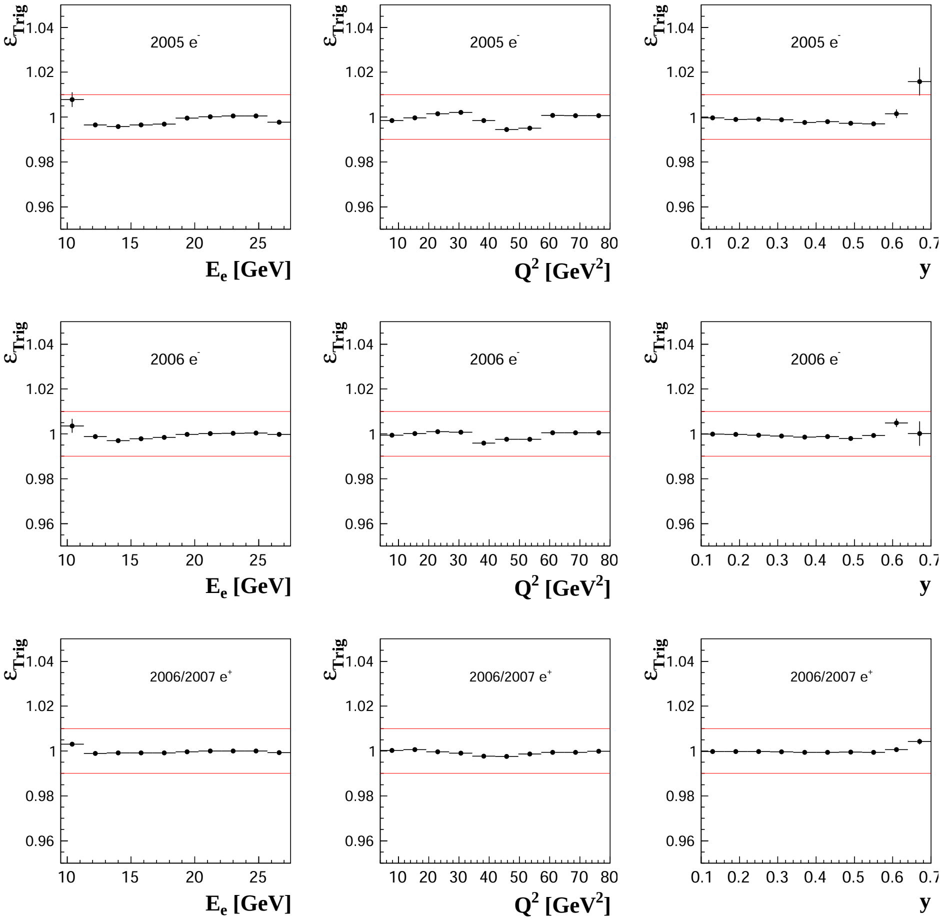

Figure 4.2: Trigger efficiency of the SPACAL component of S61 as a function of scattered electron energy E_e, Q^2 and y displayed separately for 2005 e^-, 2006 e^- and 2006/2007 e^+ run periods. The analysis sample is reweighted with the inverse of the fitted Fermi function.

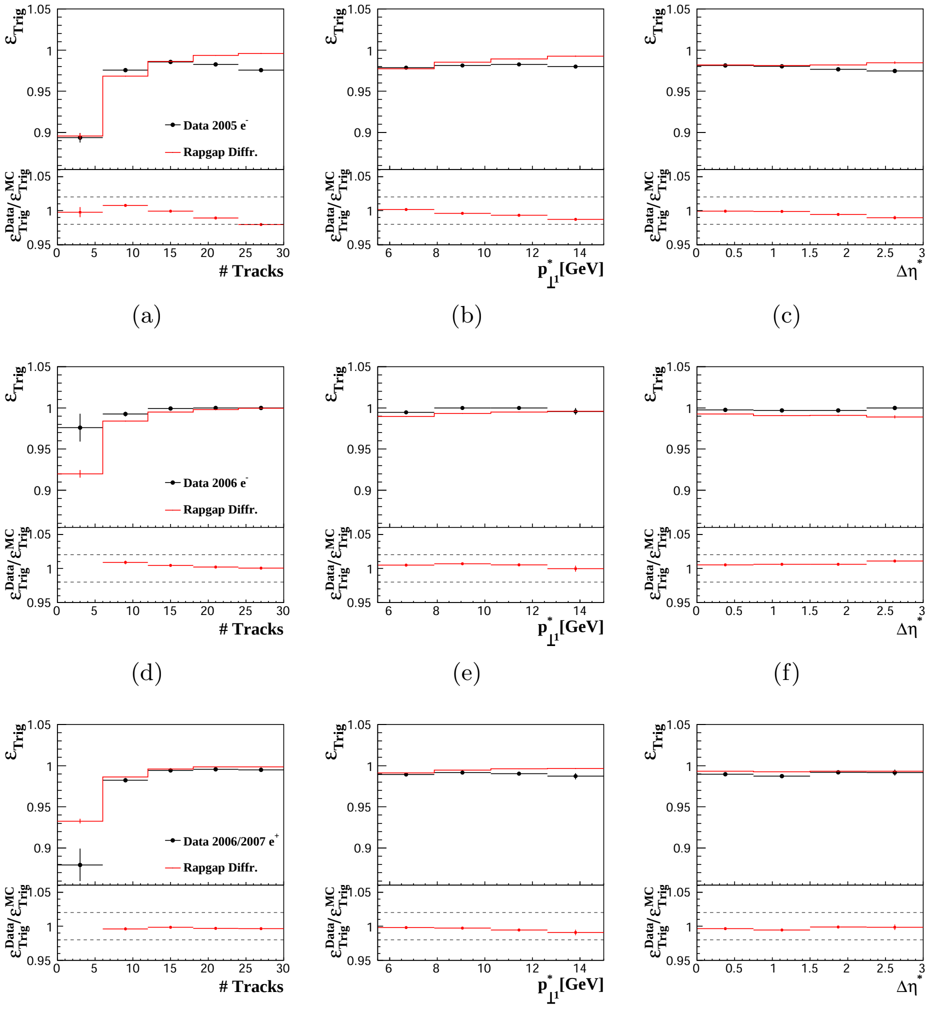

(a) (b) (c)

(d) (e) (f)

(g) (h) (i)

Figure 4.3: Trigger efficiency of the FTT part of subtrigger 61 as a function of track multiplicity, transverse momentum of the leading jet and difference in jets pseudorapidity. Comparison of data and MC FTT emulation for run periods 2005e^-. (a,b,c), 2006e^- (d,e,f) and 2006/2007e^+ (g,h,i).

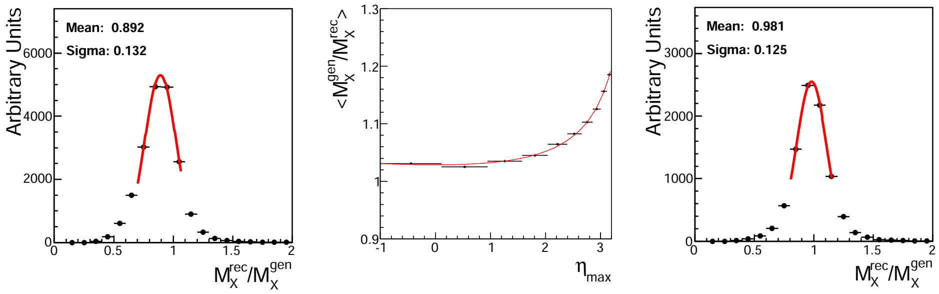

(a) (b) (c)

Figure 4.4: Hadron-detector resolution of M_X before the correction (a). Mean value of the M_X resolution as a function of η_{max} (b). The M_X resolution after the correction (c).

4.6.1 Correction of Resolution

The HFS can not be fully reconstructed due to the limited acceptance of the detector. As it can be seen in Figure 4.4 (a), approximately 10% of the HFS energy is lost at the reconstructed level compared to the model prediction at the hadron level. Hence an additional correction is applied to the reconstructed M_X for both data and MC. The mean value of the resolution M_X^{rec}/M_X^{gen} shows a non-trivial dependence on η_{max}. Figure 4.4 (b) displays the mean values $< M_X^{gen}/M_X^{rec} >$ obtained with a Gaussian fit in each bin of η_{max} with error bars corresponding to the errors of the fitted mean value. The relevant correction is than determined based on a polynomial fit to the $< M_X^{gen}/M_X^{rec} > (\eta_{max})$ dependence. The resolution improving factor appearing in the reconstruction formula 4.9 is than identified with $< M_X^{gen}/M_X^{rec} > (\eta_{max})$. The resolution of the corrected M_X is shown in Figure 4.4 (c).

4.6.2 Correlation between Detector and Hadron Level

Correlation between hadron and detector quantities and corresponding resolution are displayed in Figures 4.5 and 4.6.

The DIS quantities Q^2 and y calculated within the $e-\Sigma$ method show overall a very good resolution. The smearing in transverse momenta of the jets is a consequence of particle flow algorithm limitations and the finite calorimeter granularity. The central value of the resolution of $z_{I\!P}$ is shifted towards reconstructed values by $\sim 5\%$.

As a consequence of the smearing of jet energy, the leading jet at the reconstructed level may correspond to the subleading jet at the hadron level and vice versa. Hence the correlation and resolution of the jet azimuthal angle and pseudorapitidy are studied requiring the closest distance in the η, ϕ metrics between the hadron and detector level jets. Given a reconstructed jet with η^{rec} and ϕ^{rec}, its hadron level counterpart is chosen demanding $\min(\Delta_1, \Delta_2)$, where $\Delta_i = \sqrt{(\eta^{rec} - \eta_i^{gen})^2 + (\phi^{rec} - \phi_i^{gen})^2}$.

4.7 Comparison of Data and MC

4.7.1 Normalization of Background

The normalization of the background MC, which quantitatively describes the migration from $x_{I\!P}^{had} > 0.2$ into the measured phase space, is determined based on the inclusive DIS dijet sample, i.e. the cuts defined in Tables 4.4 and 4.5 are applied. The normalization is obtained making use of the $\log(x_{I\!P})$ distribution. The diffractive contribution is normalized to the data in the low $x_{I\!P}$ region where the non-diffractive contribution is negligible. The normalization of the sum of the diffractive and non-diffractive contribution is fixed to the normalization of the data in the region around the $x_{I\!P}$ cut. The normalization of the background sample based on the luminosity thus has to be scaled by factor of $C_{bgr} = 0.8$. Figure 4.7 shows the η_{max} and $\log(x_{I\!P})$ distributions after the normalization of MC samples.

4.7.2 Reweighting of MC

Accurate modeling of the data is further achieved by reweighting the hadron level spectra of the signal MC. In order to determine a reweighting function that is applied to hadron level quantities, a correlation matrix A between the hadron and detector level is considered. A weight value w_i in each bin i of the relevant distribution is obtained by requiring $w_i = A_{ij}^{-1} d_j$, so that the distribution in data d_i is described by MC.

A precise MC simulation of the interaction point position is of vital importance for the event kinematics reconstruction. As a consequence of the longitudinal size of the beam bunches (~ 2 cm and ~ 13 cm for electron and proton beam respectively), the vertex of the ep interaction is randomly distributed around the nominal interaction point ($z = 0$). Under the stable beam conditions, this distribution is approximately Gaussian. On the other hand, the MC z_{vtx} distribution, as simulated within the H1SIMREC, is a Gaussian distribution with a mean $< z_{vtx} = 0 >$ and a width $\sigma = 13$ cm.

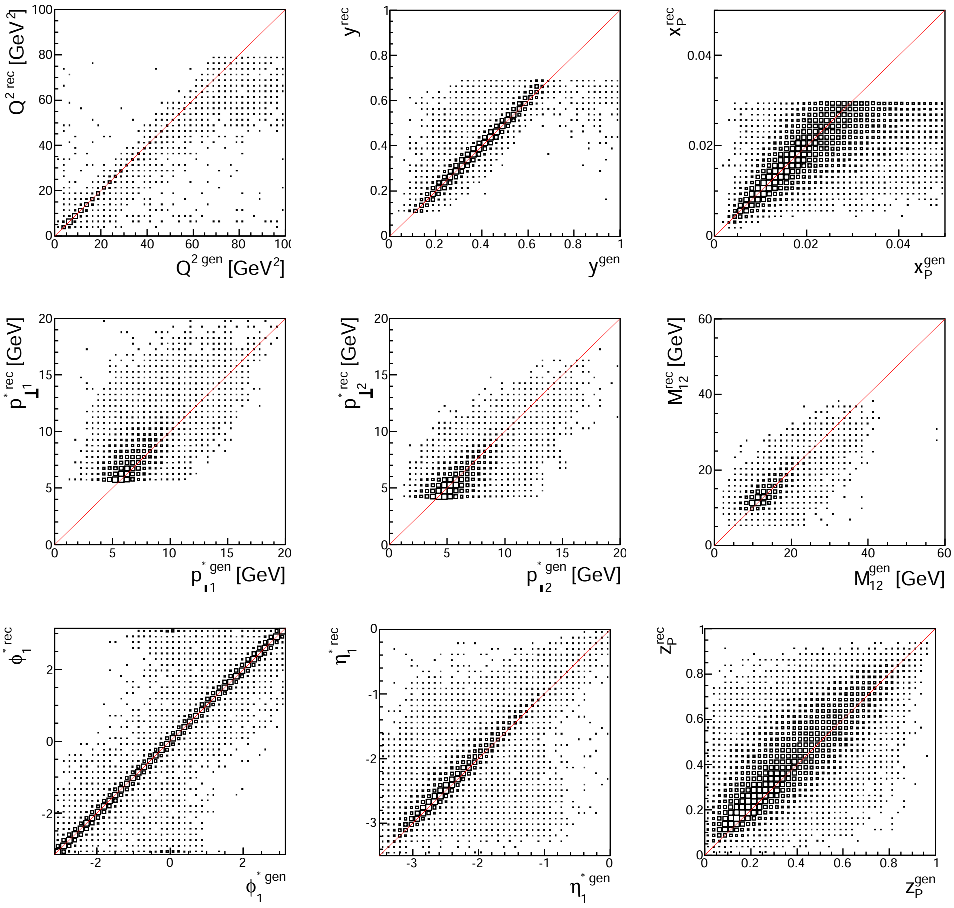

Figure 4.5: Correlations between detector and hadron level.

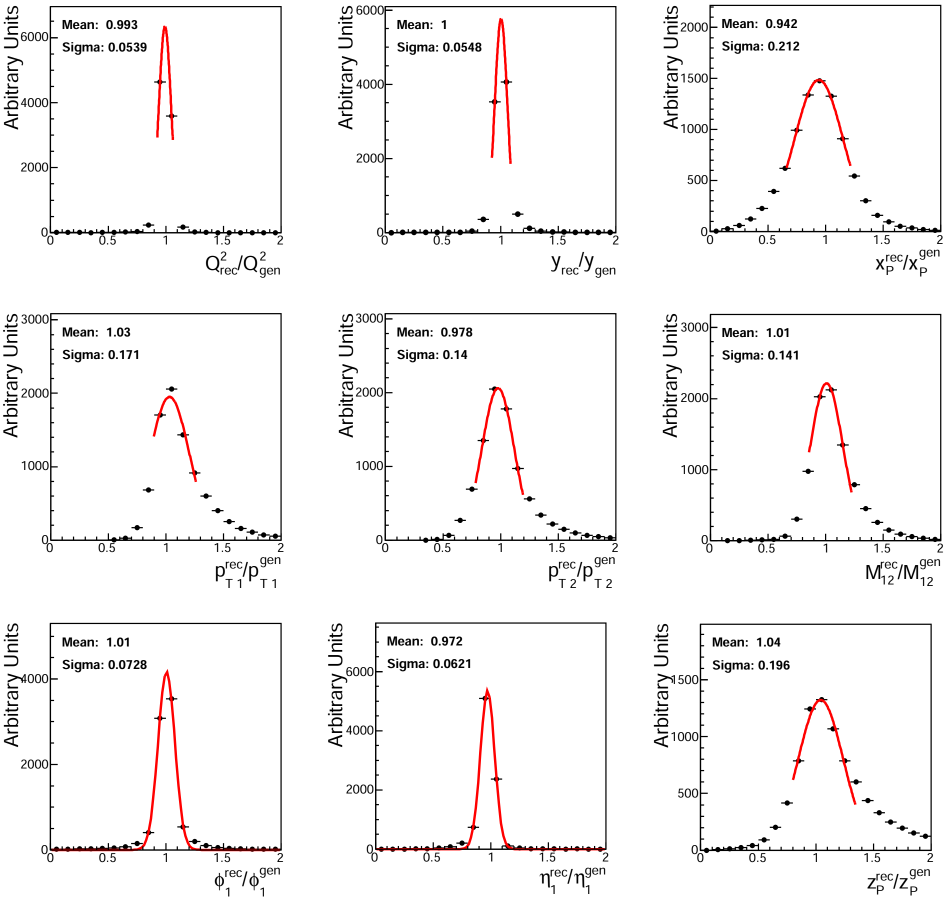

Figure 4.6: Detector resolution with respect to the hadron level.

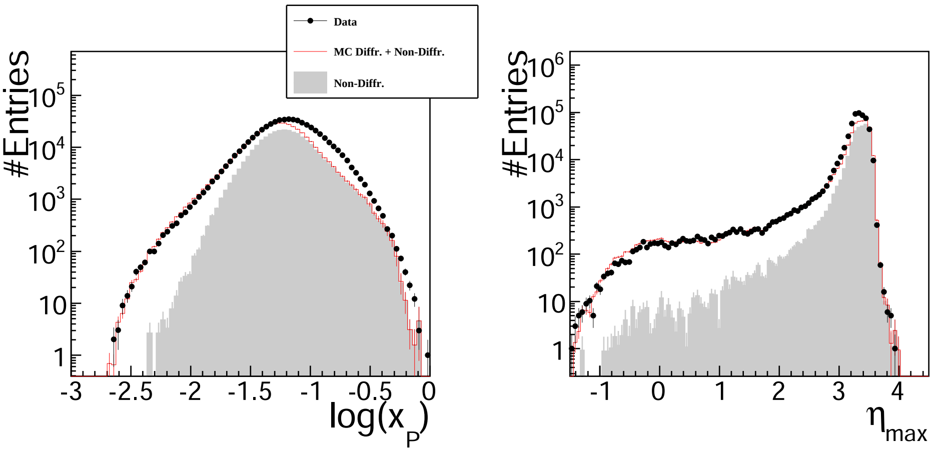

(a) (b)

Figure 4.7: Comparison of DIS dijet data and a sum of the diffractive and non-diffractive MC. The relative MC normalization is determined based on the distribution of $\log(x_{I\!P})$ (a) and is applied to the distribution of η_{max} (b).

The shape of the z_{vtx} distribution in data is modeled by means of reweighting of the MC events. The reweighting function is determined from the hadron-detector correlation matrix filled applying the full set of analysis cuts defined in Tables 4.4 - 4.6. The resulting set of weights w_i for each bin of z_{vtx}^{gen} is intercepted with a spline that is applied as the actual reweighting function.

The MC generator evaluates the QCD matrix elements up to the LO order while possible contributions from higher orders are modeled by means of initial and final state parton showers. The imprecision in the higher order QCD radiation treatment is projected not only to the overall MC normalization (the predicted cross section in MC is $\sim 10\%$ lower than in data) but also to the topology of the final state objects. While the transverse momenta of the jets agree well with the measured distributions the pseudorapidity of both jets shows significant deviation from data. The simulated MC events are therefore reweighted regarding the topology of the two jets as well as of the overall HFS, for which the variable x_γ is particularly suitable.

The reweighting function applied on x_γ^{gen} is obtained in the same manner as for the z_{vtx} reweighting.

The MC $z_{I\!P}$ distribution reweighted in x_γ still shows disagreement with data, hence an additional reweighting in $z_{I\!P}$ is performed. However, the

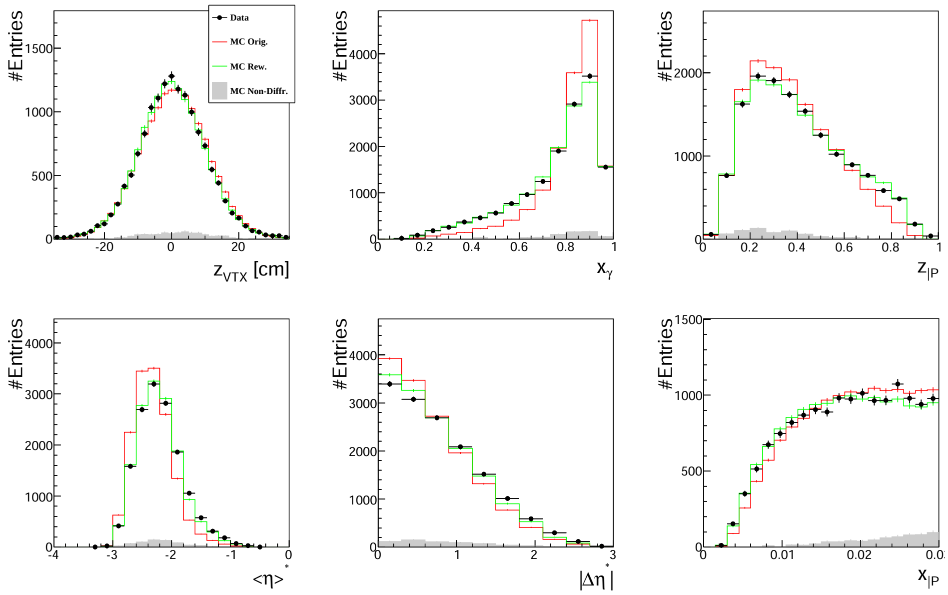

Figure 4.8: Comparison of data to the MC simulation in distributions that are significantly affected by the reweighting. Both the original and reweighted signal MC samples are displayed.

reweighting in x_γ and $z_{I\!P}$ appears not to be independent, the effects of both reweightings tend to cancel each other. In order to avoid a two dimensional reweighting and related technical complications (the correlation matrix would be replaced by a four dimensional object), the reweighting functions are determined iteratively. A sample, to which the reweighting function $w(x_\gamma, z_{I\!P}) = w^1(x_\gamma) \times w^1(z_{I\!P})$ is applied, is used again to determine a reweighting function $w^2(x_\gamma)$, etc. The reweighting functions become stable (close to one) after three iterations. The reweighting function modeling the jet and HFS topology in data reads

$$w(x_\gamma, z_{I\!P}) = \prod_{i=1}^{3} w^i(x_\gamma) \times w^i(z_{I\!P}) \tag{4.23}$$

The effect of the reweighting in z_{vtx}, x_γ and $z_{I\!P}$ is illustrated in Figure 4.8. Improvement in description of the jet psedorapidity is significant.

As the RAPGAP MC generator involves the particular fit to DPDF (H1 2006 Fit B) in its cross section calculation, the DDIS data are not accurately reproduced especially in the low Q^2 (the extracted DPDF is extrapolated into this region). Hence a three dimensional weight $w_{DPDF}(Q^2, \beta, x_{Bjorken})$, that has been determined within the H1 collaboration [42], is used.

The overall reweighting function applied on signal MC events thus provides with correction for the z_{vtx} simulation, shortcomings of the parton showers approach and indiscrepancy between the diffractive RAPGAP and the DPDF fit:

$$w = w_{DPDF} \times w(x_\gamma, z_{I\!P}) \times w(z_{vtx}) \tag{4.24}$$

The reweighted MC sample provides with satisfactory description of studied distributions.

4.7.3 Control Plots

In the following, the detail comparison of data distributions to the detector level MC distributions, so called control plots, are given.

Figure 4.9 shows the spectra related to the electron identification. The perfect description of the electron related quantities ensures reliable reconstruction of the boost vector, which is crucial for the jet finding in the γp frame.

Figure 4.10 displays a set of control plots derived from the jet quantities. Precise description of the jet transverse momenta distribution is expected even without reweighting while description of $\Delta\eta$ and $< \eta >$ is less accurate despite the full reweighting is applied. The $z_{I\!P}$ distribution is described precisely due to the reweighting.

A set of control plots related to the diffractive quantities is shown in Figure 4.11. Lack of accuracy in the forward detector response simulation is apparent.

The description of data by MC is adequate in general, except for the jet rapidity related variables, where disagreement exceeding the statistical errors of data occurs. This remaining inaccuracy is propagated to the systematic error of the measurement.

4.7.4 Energy Flow

Accuracy of the simulation of the detector response to jets can be tested by exploring the average energy flow per event of individual tracks as well as of combined track-cluster objects (particle candidates) that form HFS. The energy flow of particles surrounding a jet is studied as well.

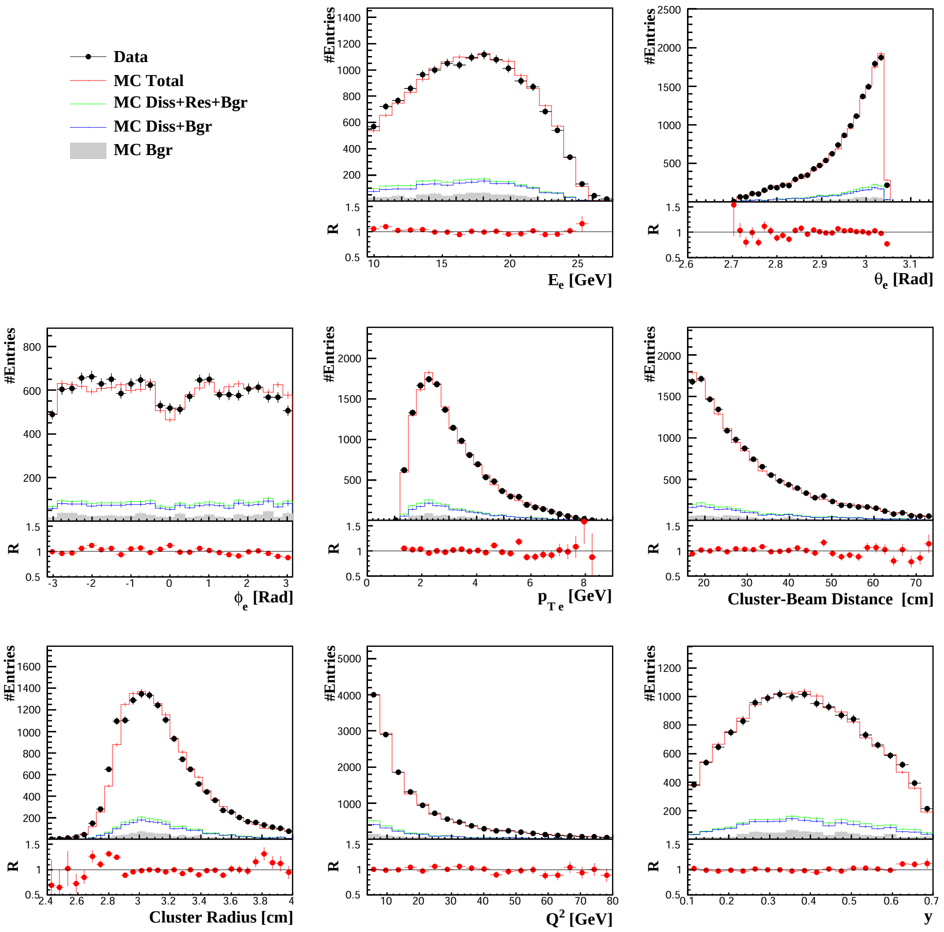

Figure 4.9: Comparison of MC simulation to data for quantities related to the scattered electron identification.

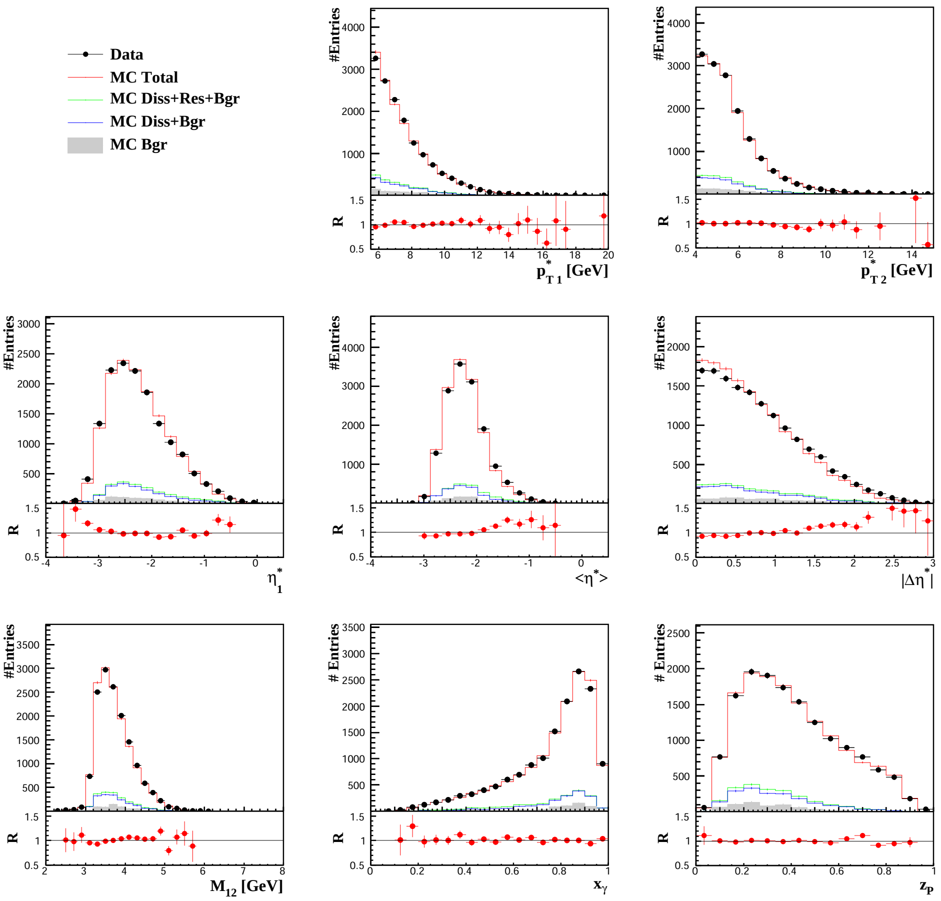

Figure 4.10: Comparison of MC simulation to data for jet quantities.

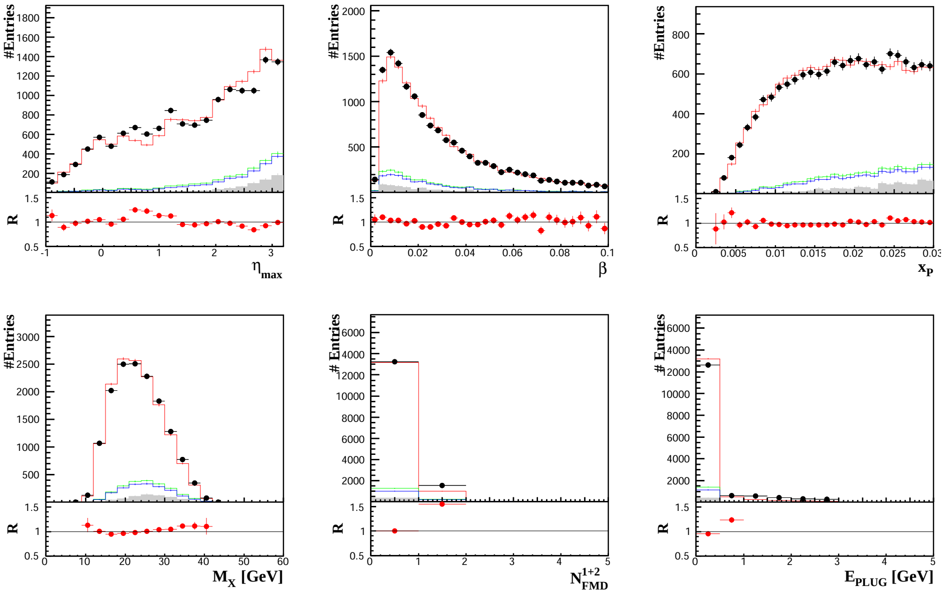

Figure 4.11: Comparison of MC simulation to data for diffractive quantities.

Figure 4.12 shows the transverse energy flow as a function of η^* of tracks and particle candidates together with the energy flow along the z axis. The values measured in data are in adequate agreement with the simulation.

A jet profile in η, resp. ϕ, is defined as the transverse energy flow of particle candidates that fulfill $|\phi^*_{jet} - \phi^*_{part}| < 1$ rad, resp. $|\eta^*_{jet} - \eta^*_{part}| < 1$. The profiles of the leading and subleading jets measured in data are adequately reproduced by the MC simulation which is demonstrated in Figure 4.13.

The precise agreement between data and MC at the level of the forward energy flow is partially a consequence of the reweighting.

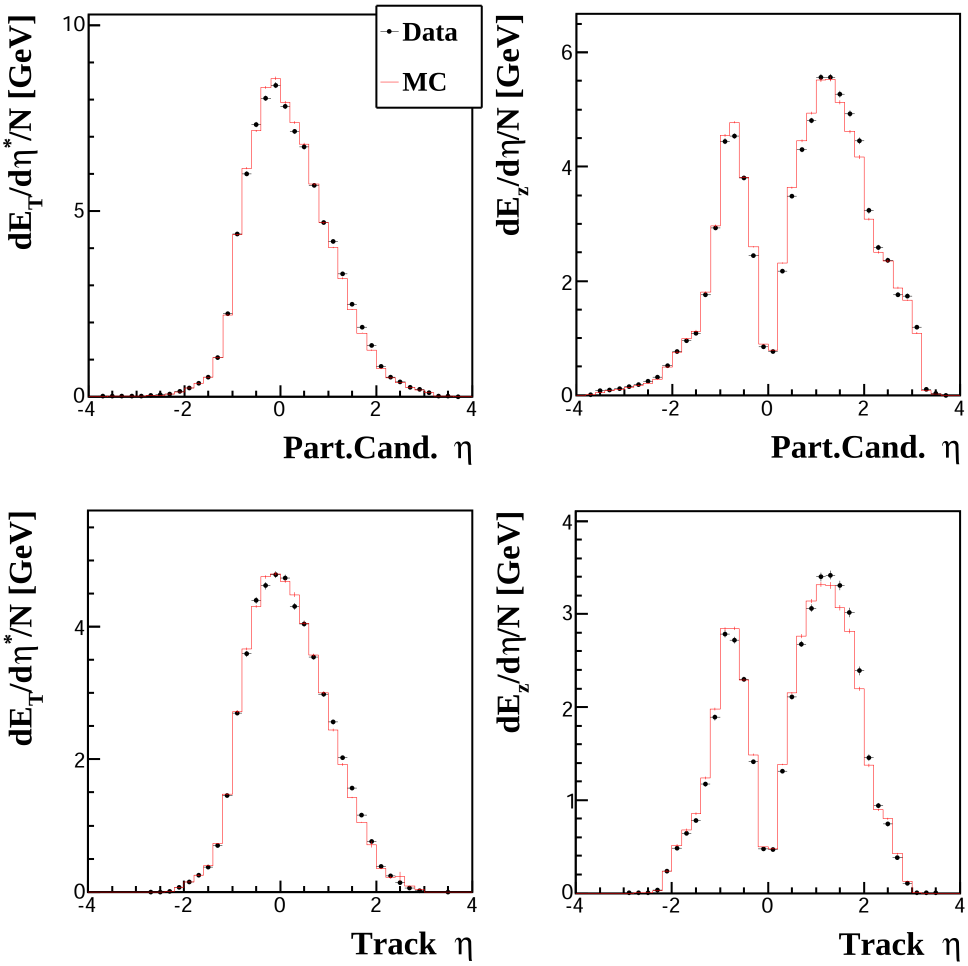

Figure 4.12: Energy flow of combined HFS objects and tracks in transverse direction and along the z-axis as a function of pseudorapidity. Data are compared to the reweighted signal MC.

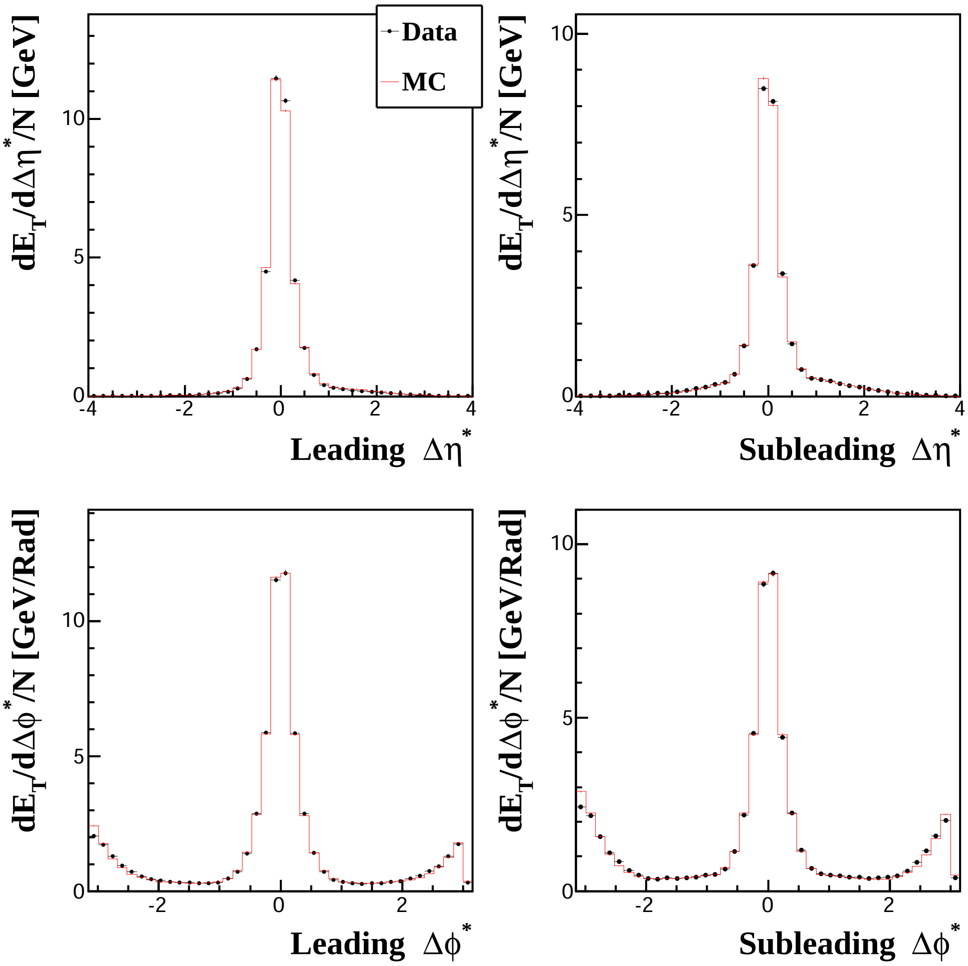

Figure 4.13: Profiles of the leading and subleading jet as a function of $\Delta\eta^* = \eta^*_{jet} - \eta^*_{part}$ and $\Delta\phi^* = \phi^*_{jet} - \phi^*_{part}$.

Chapter 5

Cross Section Measurement

The measurement of cross section of diffractive dijet production in NC DIS is presented in this chapter. The results are confronted with the NLO pQCD predictions and with diffractive dijet cross sections determined in similar measurements.

The phase space for the dijet production accessible with H1 detector, referred to as visible range, is defined by the following constrain of kinematic variables:

$$4 < Q^2 < 80 \text{ GeV}^2, \quad 0.1 < y < 0.7 \tag{5.1}$$

$$x_{I\!P} < 0.03, \quad |t| < 1, \quad M_Y < 1.6 \text{ GeV} \tag{5.2}$$

$$p^*_{T1} > 5.5 \text{ GeV}, \quad p^*_{T1} > 4.0 \text{ GeV} \tag{5.3}$$

$$-3 < \eta^*_{1,2} < 0 \tag{5.4}$$

The cross section is measured deferentially as a function of Q^2, y, $x_{I\!P}$, p^*_{T1}, p^*_{T2}, $z_{I\!P}$ and $\Delta\eta^* = |\eta^*_1 - \eta^*_2|$ and $z_{I\!P}$. The event rate N^i_{data} in bin i is unfolded to the hadron level cross section and corrected for the QED radiation effects according to

$$\frac{\mathrm{d}\sigma}{\mathrm{d}X} = \frac{N^i_{data} - N^i_{bgr}}{L.A^i} C^i_{QED} \frac{1}{\Delta^i_X} \tag{5.5}$$

where N^i_{bgr} stands for number of background events determined by the MC simulation, A_i for the acceptance in bin i and C^i_{QED} for the QED radiation effect correction factor. L denotes the integrated luminosity of the whole data sample and Δ^i_X denotes the width of the bin i. The number of observed events N^i_{data} is corrected for the trigger efficiency related to the S61 SPACAL condition while the trigger efficiency related to the S61 FTT condition is accounted for in the acceptance (see Section 4.5). The corrections applied to data are described in more detail in following sections.

5.1 QED Radiation Corrections

The initial and final state QED radiation effects may influence the measurement of the cross section in several ways. Emission of a real photon affects the reconstruction of the basic kinematic variables, especially Q^2. Further, the reconstruction of the boost vector including the radiated photon could add another transverse component with respect to the photon-proton axis faking thus an underlying QCD process. If a photon is radiated with relatively high transverse momenta it can be identified as a part of the HFS and included in the jet finding increasing thus the jet production rate. Besides the real photon emission, another effects occur due to virtual corrections which lead to running α_{em} with an impact on the cross section as a function of Q^2 in order of few percent.

The effects of the QED radiation are modeled by means of HERACLES which is interfaced to RAPGAP MC generator. HERACLES is capable of modeling emission of real photons from either initial or final state electron as well as the $e\gamma e'$ vertex correction. The effects leading to the running α_{em}, i.e. vacuum polarization and self-energy diagrams, are not part of HERACLES but are included in RAPGAP itself being thus accounted for in the acceptance.

Each measured bin i is corrected for QED radiation effect by factor C^i_{QED} given as

$$C^i_{QED} = \frac{\sigma^i_{non-rad}}{\sigma^i_{rad}} \tag{5.6}$$

with σ^i_{rad} being the cross section calculated with HERACLES interface and $\sigma^i_{non-rad}$ the cross section calculated omitting the QED effects.

The radiative corrections enhance the measured cross section by factor of $\sim 5\%$ on average. The relevant correction factors are shown in Figure 5.1

5.2 Corrections for Detector effects

The detector smearing of the underlying physics distributions is corrected for by means of the bin-by-bin method as indicated in equation (5.5). In case of the bin-by-bin correction, the precise reproduction of kinematic distributions

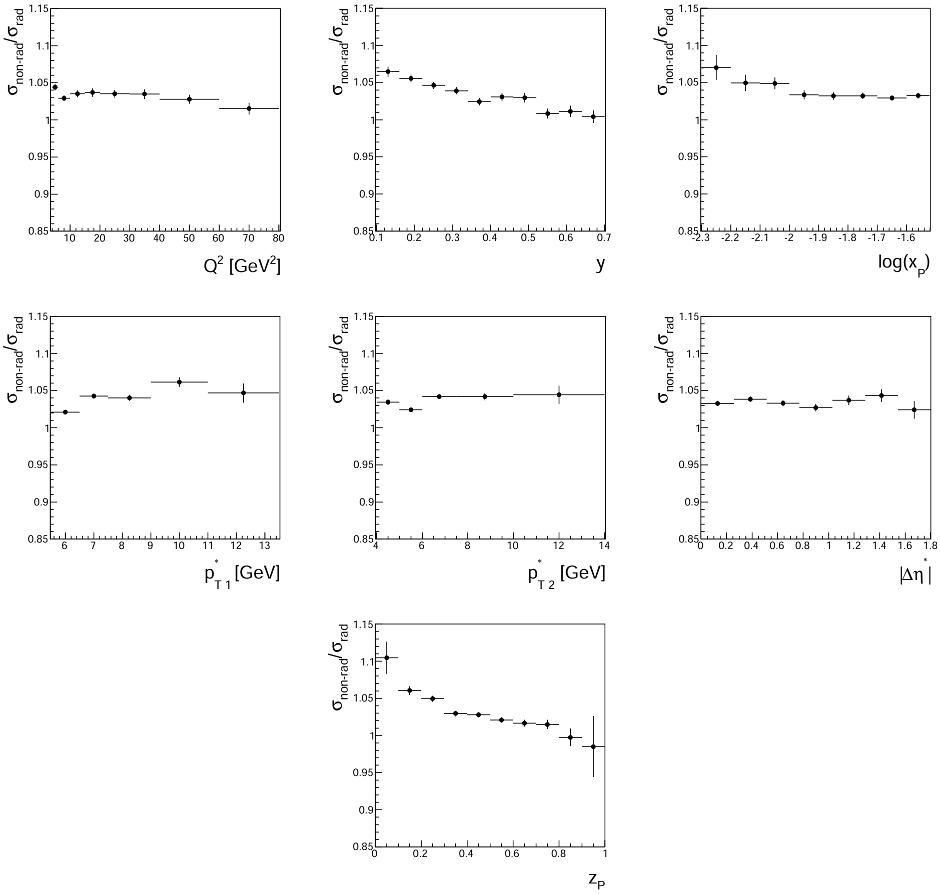

Figure 5.1: QED radiation correction factors.

in data by the MC simulation is of vital importance as well as adequate understanding of migrations between bins. The former requirement is met through the reweighting of the MC cross sections discussed in Section 4.7.2 while the latter one relays on the plausible simulation of detector effects and resolution. Besides the detector resolution, studied in Section 4.6, the migration effects are investigated in greater detail in terms of purity and stability. The following event rates are taken into account for quantifying the migrations:

- N_{rec} is the number of events reconstructed in bin i.
- N_{gen} is the number of events generated in bin i.
- N_{stay} is the number of events reconstructed and generated in bin i.
- N_{in} is the number of events reconstructed in bin i but generated in another bin of the phase space.
- N_{out} is the number of events generated in bin i but reconstructed in another bin of the phase space.
- N_{gain} is the number of events reconstructed in bin i but not generated in the phase space.
- N_{lost} is the number of events generated in bin i but not reconstructed in the phase space.

The introduced quantities are obviously related as

$$N_{rec} = N_{stay} + N_{in} + N_{gain} \tag{5.7}$$

$$N_{gen} = N_{stay} + N_{out} + N_{lost} \tag{5.8}$$

The acceptance A, purity P and stability S for each measured bin are then defined as follows:

$$A = \frac{N_{rec}}{N_{gen}} \tag{5.9}$$

$$P = \frac{N_{stay}}{N_{rec}} \tag{5.10}$$

$$S = \frac{N_{stay}}{(N_{gen} - N_{lost})} \tag{5.11}$$

Acceptance takes into account reconstruction effects as well as detector efficiency since it relates the number of events reconstructed in a particular bin to the number of events generated in the bin. Purity expresses the probability of an event generated in a particular bin to be reconstructed in the same bin. Stability quantifies the fraction of events generated and reconstructed in the same bin to the number of events generated in this bin and reconstructed within the visible phase space. The events that are reconstructed outside the visible phase space are not included in the stability definition since they are already treated within the acceptance.

The values of purity, stability and acceptance in the binning chosen for the measurement are shown in Figure 5.2. The total purity is at level of 45 % and the total acceptance of 80 %. The purity remains stable and confidentially high for Q^2 and y distributions, while it shows rather strong dependence for variables calculated directly from HFS and jets, which is expected due to the poor resolution of the relevant variables. The acceptance in the lowest Q^2 bin is very low. The decrease can be connected with a flow of events from the region bellow the Q^2 cut into the first bin. This can be cured by involving a more sophisticated unfolding procedure, based on a least square fit with Tikhonov regularization [43], than the bin by bin correction used here.

5.3 Hadronization Corrections

In order to compare the measured cross section to the NLO pQCD prediction, which is calculated at level of partons, the effect of hadronization has to be accounted for.

The relevant correction factors are calculated making use of the dedicated MC samples which employs different models of parton showers. The hadronization corrections can be readily applied only if the correspondence between the parton and hadron level quantities is accurate. Figure 5.3 resp. 5.4 shows the parton to hadron level correlation resp. resolution for the quantities of interest. The variables calculated from the measurement of the scattered electron are insensitive to the hadronization effects. The mass of HFS M_X remains same on both levels due to momentum conservation therefore the effect on the $x_{I\!P}$ distribution is significantly low. On the other hand, the jet finding accounts for all objects contained in the HFS, which is different on the parton resp. hadron level. The correspondence between variables derived from the jet measurement, e.g. $z_{I\!P}$ is consequently less accurate. However, the resolution of 15% still allows for reliable correction of the partonic cross section to the hadron level.

Although the signal MC involves the LLPS approach to the parton show-

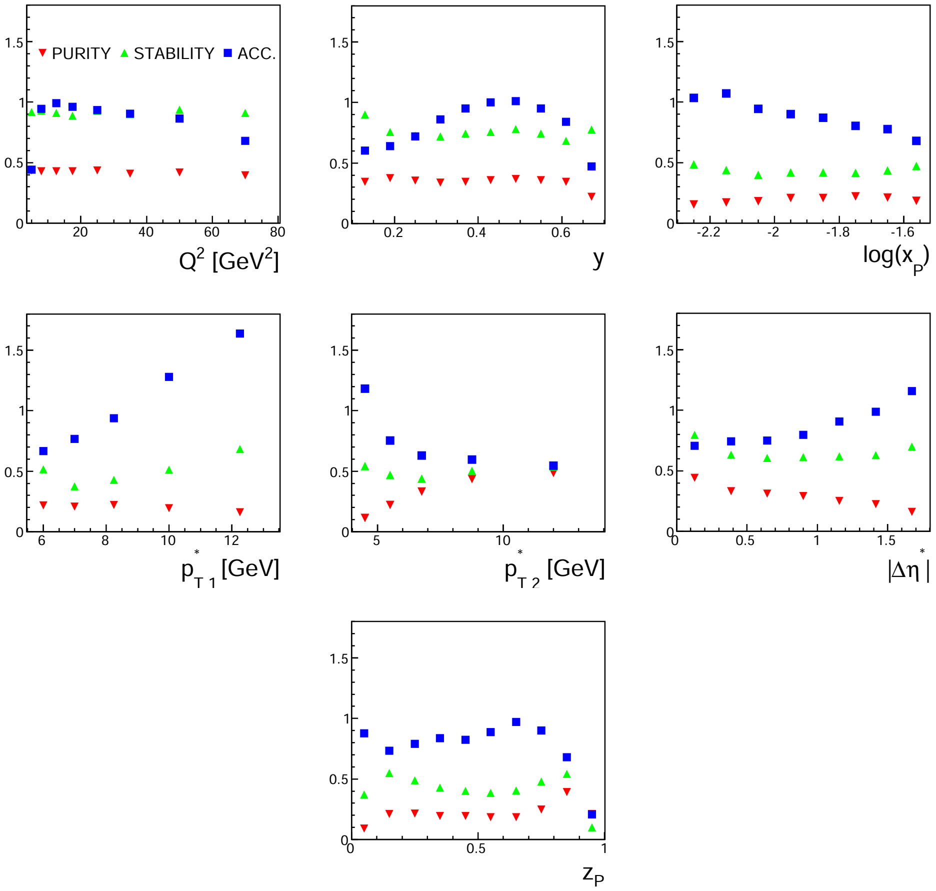

Figure 5.2: Acceptance, purity and stability.

ers, the hadronization corrections are additionally studied with a sample involving another approach, the Color Dipole Model (CDM) (see Section 4.2.1). The cross section calculated with either parton showers model should agree with the cross section calculated by means of nlojet++, for which the parton level of RAPGAP is reweighted to the nlojet++ calculation in $z_{I\!P}$. The agreement after the reweighting is illustrated in Figure 5.5.

The hadronization correction factor C^i_{had} in a bin i is determined as a fraction the cross section on the hadron level σ^i_{had} to the cross section on the parton level σ^i_{part}:

$$C^i_{had} = \frac{\sigma^i_{had}}{\sigma^i_{part}} \tag{5.12}$$

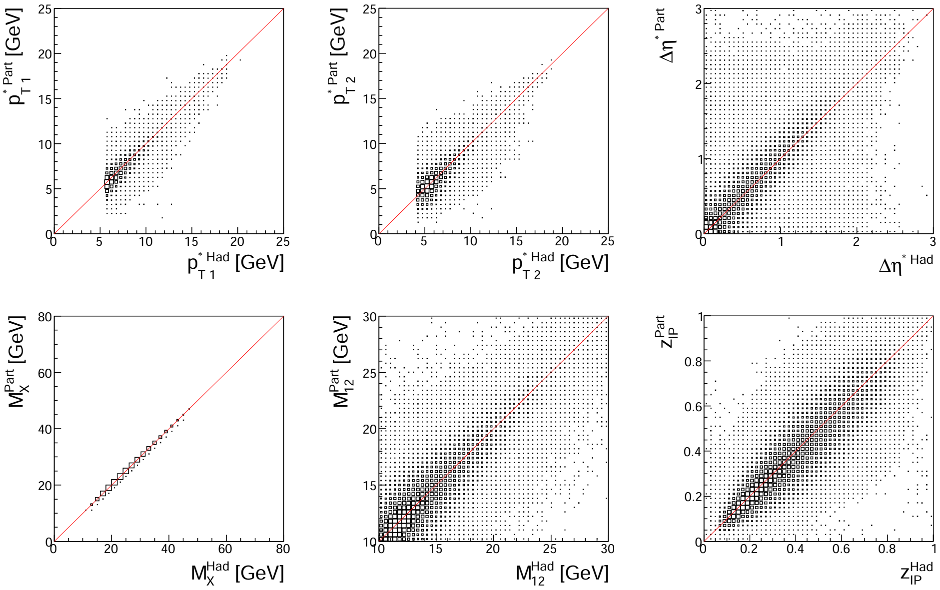

Figure 5.3: Correlation between parton and hadron quantities.

The actual correction factor is then taken as an average value of the factors calculated with two different parton shower models $C^i_{had} = (C^{iLLPS}_{had} + C^{iCDM}_{had})/2$. The uncertainty on the correction factors is considered as the maximum difference between the two parton showers models and the central value

$$\Delta C^i_{had} = \max(|C^{iLLPS}_{had} - C^i_{had}|, |C^{iCDM}_{had} - C^i_{had}|) \tag{5.13}$$

The hadronization corrections for both parton shower models as well as the central values are shown in Figure 5.6. The correction enhances the total parton level cross section by 10%. The average value of the uncertainty of the correction factors is $\sim 9\%$.

5.4 Uncertainties of Measurement

The uncertainty of the cross section determination is dominated by the experimental systematic error due to the relatively large number ($\sim 10^3$) of reconstructed dijet events. Sources of systematic uncertainty given by the detector limitations as well as by the model dependence of the measurement are considered.

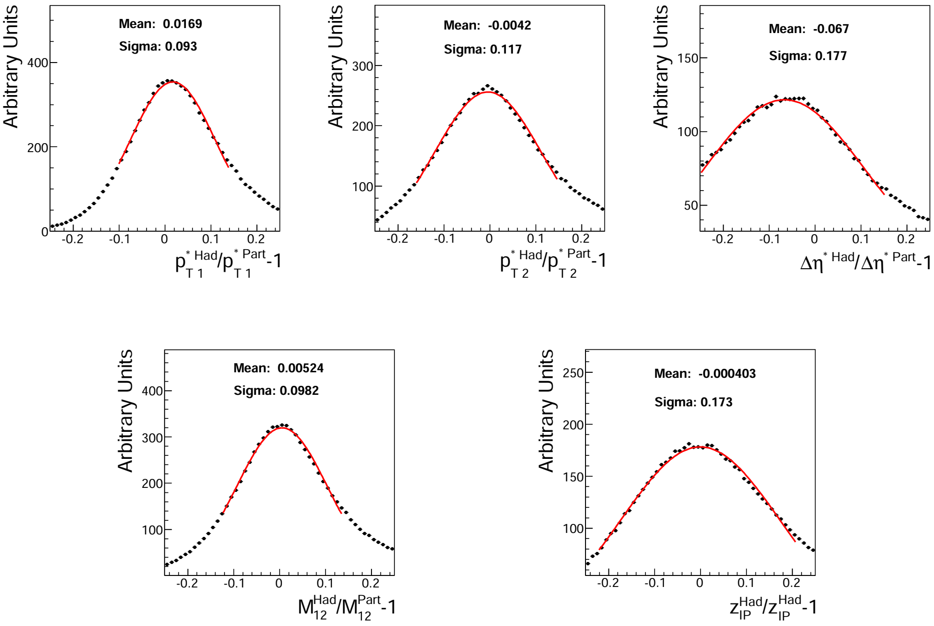

Figure 5.4: Resolution between parton and hadron quantities.

5.4.1 Detector Systematic Uncertainties

The intrinsic resolution and calibration of the detector impose imprecision in basic kinematics reconstruction (electron and HFS). The corresponding bias on the measured cross section is explored via variation of the relevant quantities on the detector level of the MC simulation.

The precision of the scattered electron energy measurement is $\sim 2\%$ which turns into $\sim 1\%$ error of the total cross section determination.

The angle of the scattered electron is experimentally determined with precision of 1mrad. Variation of the electron angle is translated into the error of $\sim 1\%$ on the total cross section.

In general, a measurement requiring jets in the final state is, sensitive to the energy measurement of HFS. The H1 detector allows for separation of electromagnetic and hadronic showers followed by reconstruction and calibration of single HFS object within the precision of 2% in the energy scale. The uncertainty of the HFS energy determination is thus regarded by varying energy of each object contained in HFS by ±2%. The resulting error of 4% on the total cross section measurement is the dominating detector systematic error.

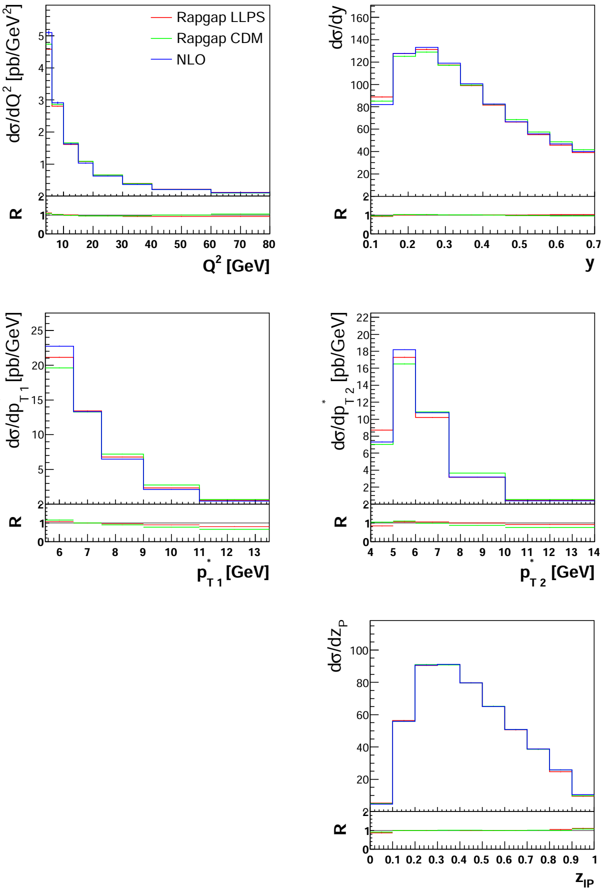

Figure 5.5: The Rapgap MC on the parton level compared to the NLO QCD prediction. The MC cross section is reweighted to NLO in $z_{I\!P}$.

The uncertainties originating in the electron and HFS measurement imprecision are treated as uncorrelated, e.i. evaluated for each measured bin separately. The efficiency of the trigger S61 and the precision of the luminosity measurement introduces source of the correlated uncertainties as they are expected to be independent from a particular kinematic variable. The trigger efficiency related to the SPACAL, resp. FTT, condition of the S61 subtrigger introduces the error of 1%, resp. 2% on the normalization of the cross section. The experimental error of the luminosity determination, which is 2.5% for the selected data sample, is accounted for as the additional uncertainty on the normalization.

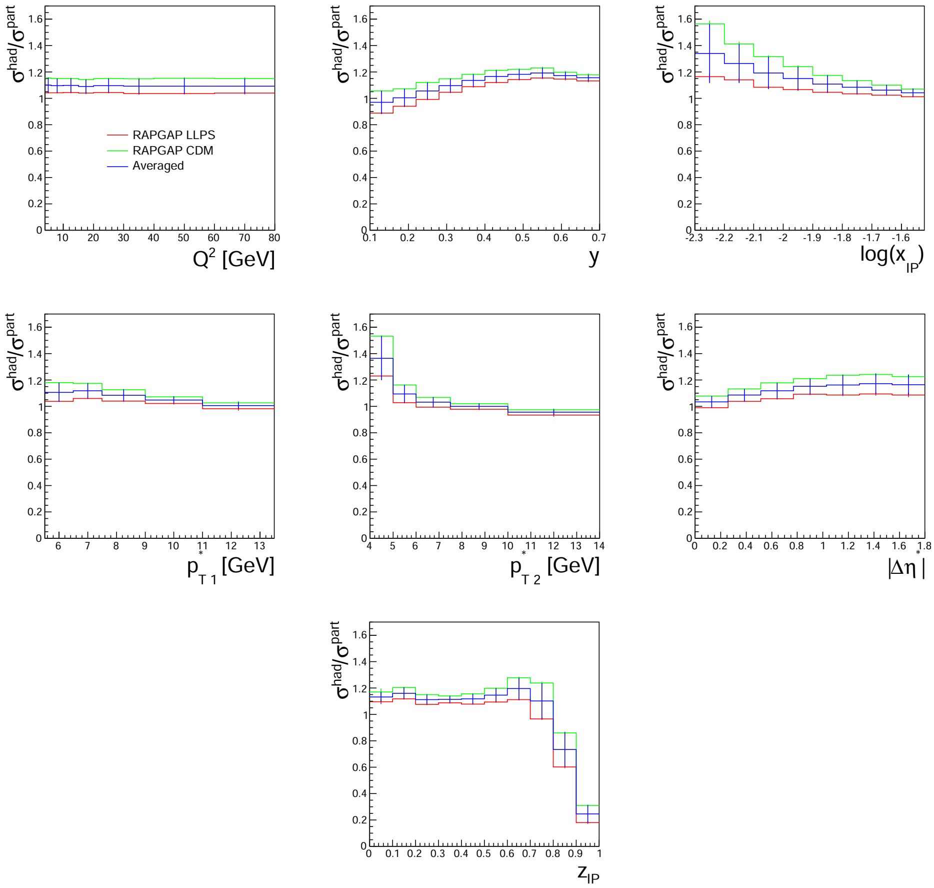

Figure 5.6: Hadronization correction factors.

The total cross section determination is biased with the error of 6% due to the detector restraint.

5.4.2 Model Systematic Uncertainties

Besides the uncertainties imposed by the experimental precision, the cross section measurement is also biased by the limitations of the involved model as well as the detector simulation.

The error of the translation of the measured event rate to the hadron level cross section is accounted for by varying the shapes of the distributions p^*_{T1}, Q^2, $x_{I\!P}$, β, t, $|\Delta\eta|$, x_γ and $z_{I\!P}$ within the statistical errors of the data. The Q^2 distribution is reweighted by $\log^{\pm 0.2}(Q^2)$, the $x_{I\!P}$ distribution by $x_{I\!P}^{\pm 0.05}$, the β distribution by $\beta^{\pm 0.01}(1-\beta)^{\pm 0.01}$, the p^*_{T1} distribution by $p^{*\pm 0.4}_{T1}$ and $\Delta\eta$ distribution by $(1.5+\Delta\eta)^{\pm 0.5}$. The slope of the t distribution is varied within the error of the fitted value [44], for which the weight of form $e^{\pm t}$ is applied. Since the MC is accommodated to the data by reweighting in x_γ and $z_{I\!P}$, the additional uncertainty is studied by reweighting by $x_\gamma^{\pm 0.15}$ and $z_{I\!P}^{\pm 0.15}$ The values of uncertainty corresponding to the shape variations are listed in Table 5.1. The total uncertainty stemming from the detector to hadron level transition, calculated as a square sum of the individual contributions, is 4%.

The effective selection of the diffractive events in data by the LRG method requires an accurate MC simulation of the forward energy flow. The accuracy of the simulation is studied by direct tagging of the elastically scattered proton in the H1 detector. Whereas the RAPGAP simulation is found to agree with data within 30% [45], the events lying in the phase space given by (5.1- 5.4) but rejected by the LRG criteria defined in Table 4.5 are reweighted by factor of ±30%. The LRG selection inefficiency is thus propagated into the uncertainty of 7%.

An additional source of the model uncertainty is related to possible migrations of non-diffractive events into the measured $x_{I\!P}$ range. Hence the normalization of the background MC sample is varied by 50%, which affects the total cross section by less than 0.5%.

The overall systematic uncertainty stemming from the model inaccuracy is 9%. The description of the kinematic distributions in data within the model originated errors is illustrated in Figure 5.7.

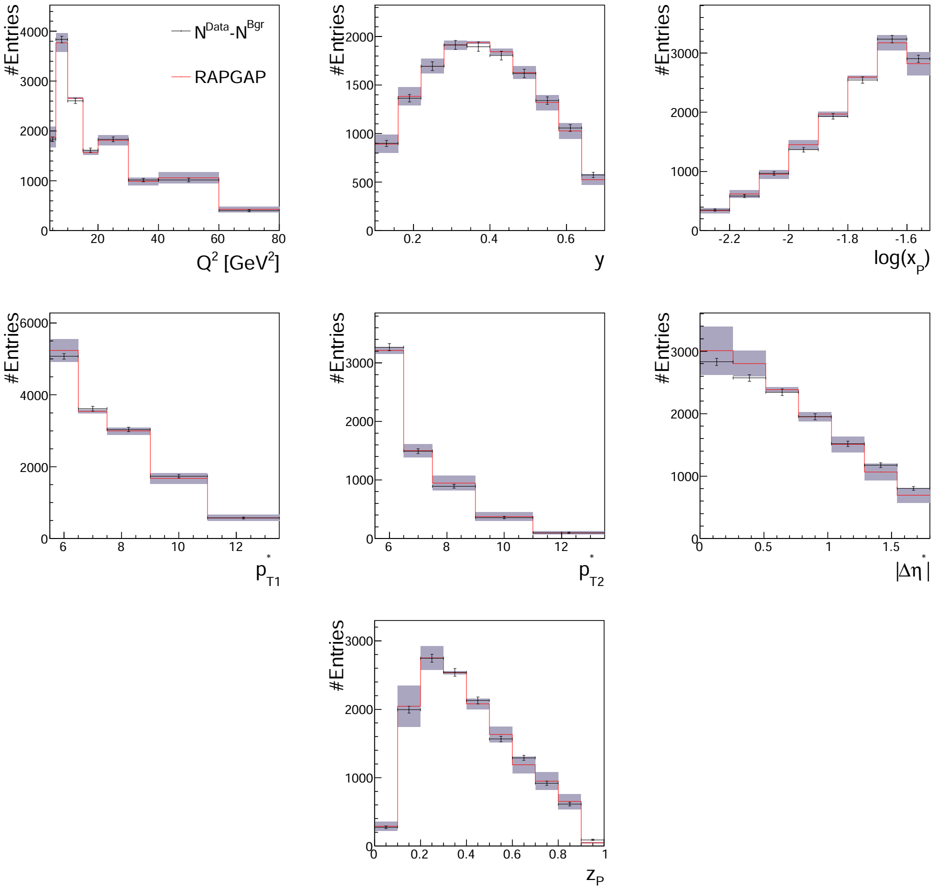

Figure 5.7: Comparison of kinematic distributions in data and reweighted RAPGAP. The model systematic errors are displayed as the shadow band around MC values. The non diffractive background is statistically subtracted from the data.

5.4.3 Statistical uncertainty

The statistical uncertainty enters the measurement as a consequence of a finite number of events determining the relevant quantities and is given as the first momentum of Poisson distribution, i.e. counting N events is biased with the error of $\sqrt{N}$. Although the MC samples are populated with statistics ~ 10 times higher than data the statistical error of the MC can not be safely neglected especially in some particular bins. Moreover, the

Varied Distribution	Weight Function	Error
p^*_{T1}	$p^{*\pm 0.4}_{T1}$	3.1 %
t	$e^{\pm t}$	2.6 %
$\Delta\eta^*$	$(1.5 + \Delta\eta)^{\pm 0.5}$	2.0 %
Q^2	$\log^{\pm 0.2}(Q^2)$	1.1 %
$z_{I\!P}$	$z^{\pm 0.15}_{I\!P}$	2.0 %
x_γ	$x^{\pm 0.15}_\gamma$	0.6 %
β	$\beta^{\pm 0.01}(1-\beta)^{\pm 0.01}$	0.5 %
$x_{I\!P}$	$x^{\pm 0.05}_{I\!P}$	0.6 %
Total		9.1 %

Table 5.1: Overview of systematic uncertainties of the unfolding of data to the hadron level.

migration between bins may cause additional rise in statistical error. The acceptance can be expressed as a function of uncorrelated quantities N_{stay}, N_{in}, N_{out} and N_{lost}, which are directly related to the migrations, combining the equations 5.7 and 5.8. The statistical error of MC is evaluated as the uncertainty on the acceptance according to

$$\sigma_A^2 = (\frac{\partial A}{\partial N_{stay}})^2 \sigma_{stay}^2 + ... \tag{5.14}$$

and is added to the statistical error of the data in quadrature.

5.4.4 Summary of uncertainties

The model uncertainties, including the LRG selection inefficiency, are at level of 9 % and represent the dominant contribution to the error of the measurement. The detector induced uncertainties contribute at level of 2.8% while the statistical uncertainty of 1 % is relatively small. The integrated cross section determination is biased with the total experimental error of 11 %.

5.5 Results

The integrated cross section of the DDIS dijet production measured in the phase space given by (5.1) is determined to be

$$\sigma(ep \to e' X_{dijet} Y) = 63.4 \ \pm \ 0.7 \ (stat) \ \pm \ 6.7 \ (sys) \text{ pb} \tag{5.15}$$

The above value represents the cross section at the level of stable hadrons corrected for QED radiation effects and the trigger efficiency.

5.5.1 Comparison to NLO Calculations

Figures 5.8 and 5.9 show comparison of the single differential diffractive dijet cross section measured as a function of Q^2, y, $x_{I\!P}$, p^*_{T1}, p^*_{T2}, $\Delta\eta^*$ and $z_{I\!P}$ to the NLO QCD predictions.

The NLO QCD cross sections are calculated by means of the nlojet++ program which is adjusted to diffractive processes as described in Section 2.5. The effects of hadronization are accounted for by application of the hadronization correction factors derived in Section 5.3. The uncertainty of the prediction is given by variation of the chosen scale $\mu^2 = Q^2 + < p^*_T >$ in range from $\mu^2/4$ to $4\mu^2$ resulting in the average uncertainty of $\sim 35\%$. Additional source of the uncertainty is introduced due to the errors of the PDF fit parameters. The resulting uncertainty on the integrated cross section is at level of $\sim 40\%$. The scale and PDF uncertainties are added in square. The uncertainty of the hadronization correction factors, which is on average $\sim 8\%$, is propagated to the total NLO prediction uncertainty in every bin of the measurement. The combined uncertainty is displayed in Figures 5.8 and 5.9. as an error band around the central value.

The total cross section of the diffractive dijet production in DIS calculated in NLO QCD is

$$\sigma^{part}_{ep\to q\bar{q}} = 51.3^{+18.3}_{-11.5} \text{ (scale)} \pm 10.3 \text{ (fit) pb} \tag{5.16}$$

The total cross section with the hadronization correction applied yields

$$\sigma^{had}_{ep\to q\bar{q}} = 56.2^{+20.3}_{-12.9} \text{ (scale)} \pm 11.3 \text{ (fit)} \pm 2.8 \text{ (had.) pb} \tag{5.17}$$

The value predicted utilizing the H1 2006 Fit B underestimates the total cross section measured at hadron level by about 12%, however, the difference does not exceed the scale and PDF uncertainty of the prediction.

The differential cross section measured as a function of Q^2 shows satisfactory agreement with the NLO prediction except of the lowest bin where

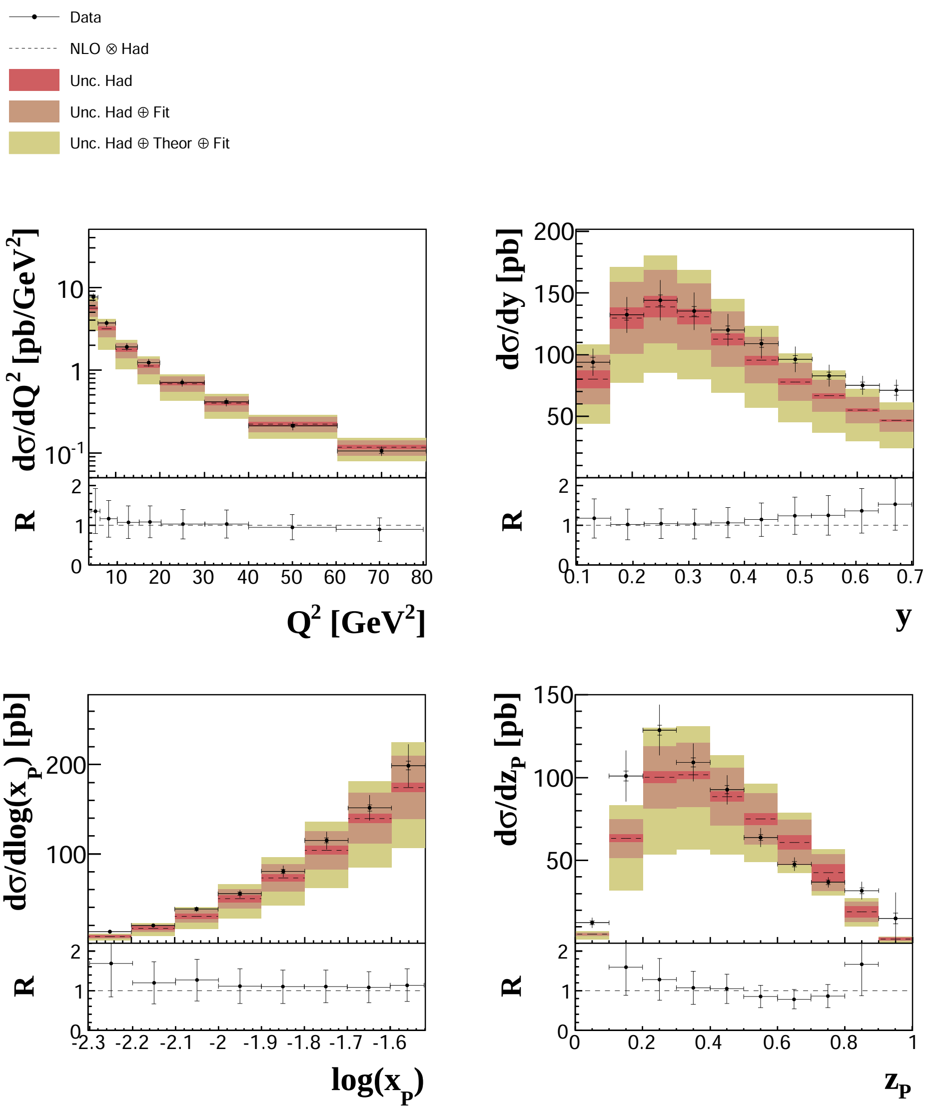

Figure 5.8: Comparison of the data to the NLO QCD predictions based on H1 2006 Fit B and corrected for the hadronization effects. The inner error bars of the data points represent the statistical errors and the outer error bars represent the systematic and statistical errors added in quadrature. The inner band around the NLO QCD predicted values represents the hadronization error, the broader band represent the DPDF fit uncertainty with hadronization error propagated and the outer band represent the total uncertainty of the prediction. The lower part of each plot displays the ratio of measured values to the predictions.

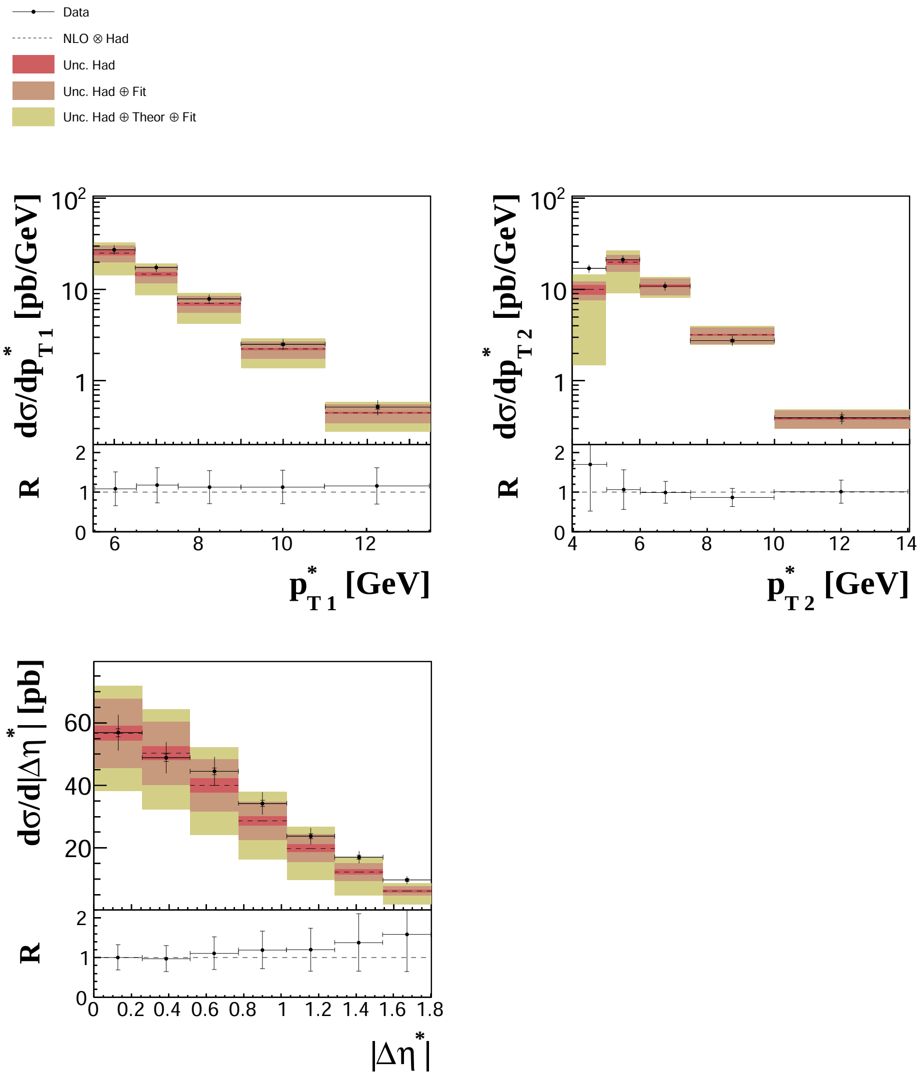

Figure 5.9: Comparison of the data to the NLO QCD predictions based on H1 2006 Fit B and corrected for the hadronization effects. The inner error bars of the data points represent the statistical errors and the outer error bars represent the systematic and statistical errors added in quadrature. The inner band around the NLO QCD predicted values represents the hadronization error, the broader band represent the DPDF fit uncertainty with hadronization error propagated and the outer band represent the total uncertainty of the prediction. The lower part of each plot displays the ratio of measured values to the predictions.

the predicted value is slightly lower than the data. The differential measurement in y is in excellent coincidence with the prediction for $y <\sim 0.45$ while for higher y, the NLO calculation underestimates the measured data. The shapes of the $x_{I\!P}$ and p_{T1} differential cross sections are well described by the NLO calculation. A good agreement between the NLO calculation and the measurement can be also observed in the p_{T2} single differential measurement. The cross section measured differentially in $z_{I\!P}$ is properly described by the NLO calculation. One should take into account that in the region of $z_{I\!P} > 0.8$, the H1 2006 Fit B is not determined from inclusive measurements and is extrapolated in that region.

In general, the measured differential cross sections are in good agreement with the NLO QCD prediction.

5.5.2 Comparison with Other Measurements

The measured cross sections are further compared to results of similar measurements - first to the measurement of dijet production involving HERA I data with the LRG method of selection of diffractive events and second to the measurement involving the HERA II data with the direct proton tagging via the Forward Proton Spectrometer (FPS).

LRG Analysis of HERA I Data

The cross section of the diffractive dijet production determined using HERA I data [46] is

$$\sigma_{ep\to q\bar{q}} = 52 \;\pm 1 \text{ (stat.) } {}^{+7}_{-5} \text{ (syst.) pb} \tag{5.18}$$

which is lower than the presented value (5.15) but is in agreement within uncertainties of both measurements. Figures 5.10 and 5.11 show the differential cross section compared to the values given in [46]. The shapes of the distributions agree rather well, although a small difference of about $\sim 15\%$ in normalization is observed.

FPS Analysis of HERA II data

The dijet production in diffractive NC DIS is also studied in [47], where diffractive events are reconstructed making use of direct leading proton detection by means of FPS.

Figure 5.12 displays the comparison of the dijet differential cross section as a function of $\log(x_{I\!P})$ measured with the leading proton method [47] to the values obtained by means of the LRG method [46]. Additionally, the

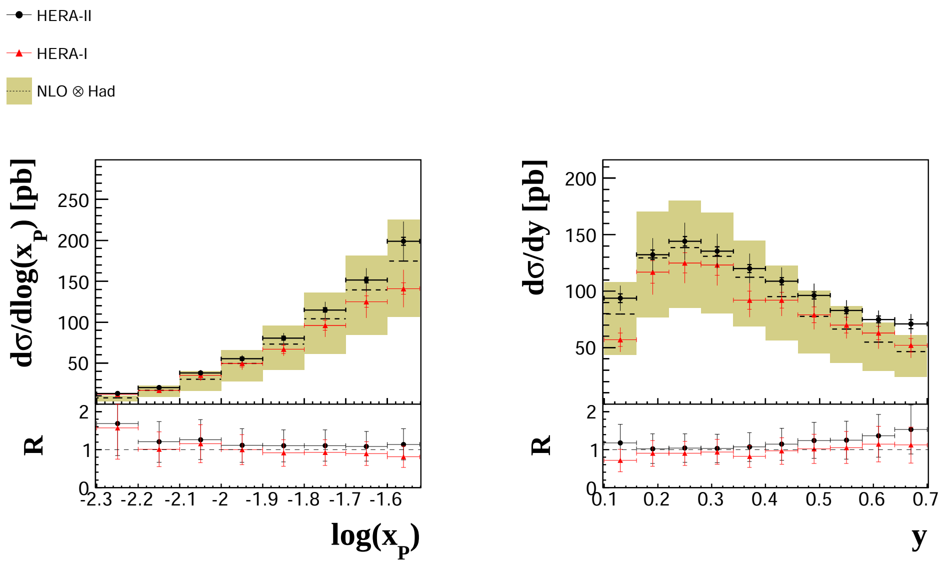

Figure 5.10: Comparison of the current measurement (black points) with the measurement performed with the HERA I data [46] (red points) in variables $\log(x_{I\!P})$ and y. The inner error bars of the data points represent the statistical errors and the outer error bars represent the systematic and statistical errors added in quadrature. The NLO QCD predictions based on H1 2006 FitB and corrected for the hadronization effects are also depicted; the error band represents the total theory uncertainty of the prediction. In the lower part of each plot, the ratio of the data to the NLO prediction is displayed for the current measurement (black points) and for the HERA I analysis (red points).

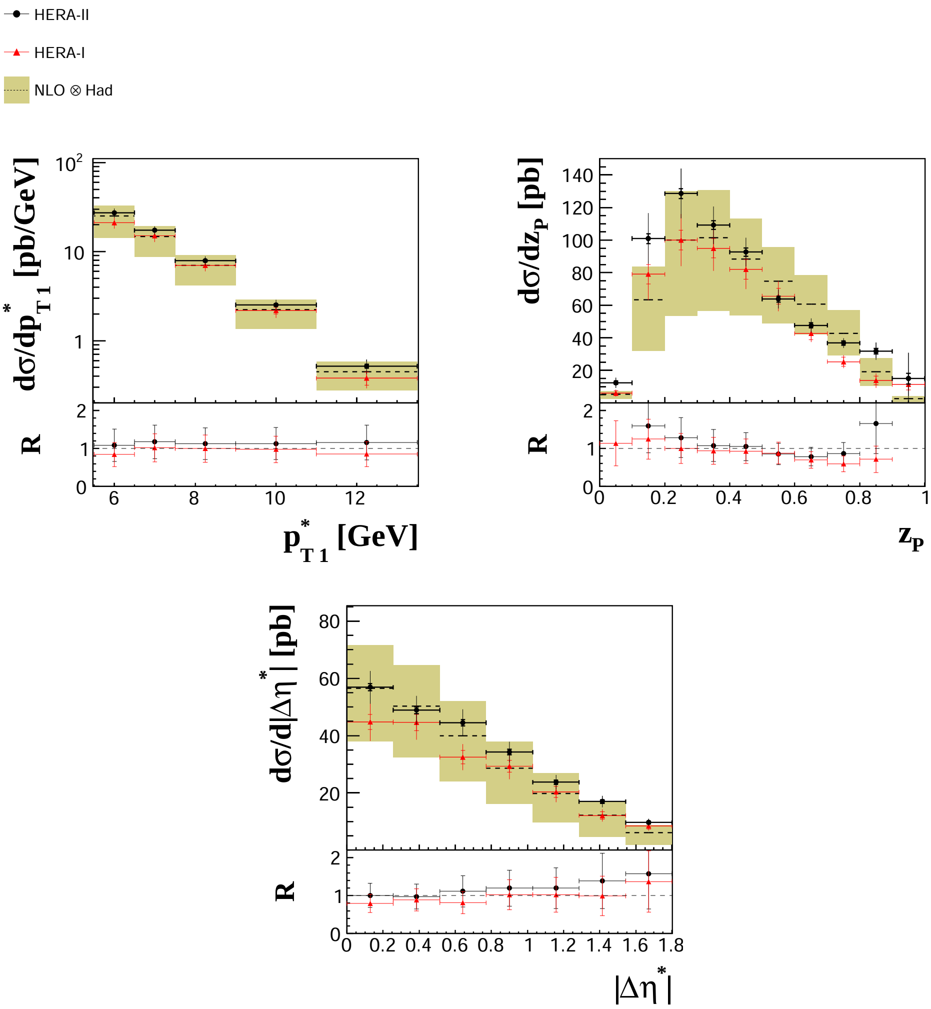

Figure 5.11: Comparison of the current measurement (black points) with the measurement performed with the HERA I data [46] (red points) in variables p^*_{T1}, $z_{I\!P}$ and $\Delta\eta^*$. The inner error bars of the data points represent the statistical errors and the outer error bars represent the systematic and statistical errors added in quadrature. The NLO QCD predictions based on H1 2006 FitB and corrected for the hadronization effects are also depicted; the error band represents the total theory uncertainty of the prediction. In the lower part of each plot, the ratio of the data to the NLO prediction is displayed for the current measurement (black points) and for the HERA I analysis (red points).

results of this analysis are depicted. The both cross sections determined within the LRG method are scaled down by factor of 1.2, since the leading proton reconstruction technique excludes events with a low mass dissociative system. The difference between the direct tagging of the leading proton and the LRG selection is measured to be 20 % [48] in terms of the hadron level cross section.

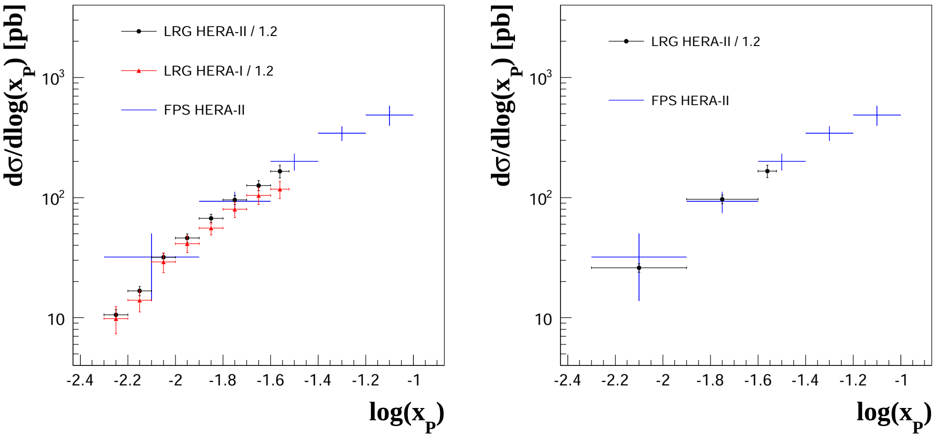

Figure 5.12: Diffractive dijet differential cross section as a function of $\log(x_{I\!P})$ compared with the HERA I dijet data measured by the LRG technique [46] and with the HERA II dijet data measured using FPS [47]. In the right plot, comparison of the LRG data obtained in this analysis to the FPS data is given in the same binning in the first two bins.

The results presented in the current measurement differ from the HERA I analysis mainly in high $x_{I\!P}$ region. One should take in mind that the system of forward detectors changed in the HERA II period in comparison with HERA I. The leading proton analysis relays fully on the FPS information and is independent from the forward detector information. The presented dijet differential cross section in $\log(x_{I\!P})$ shows rather better agreement with the FPS measurement from the HERA II run period than the analysis of the HERA I data [46].

Chapter 6

Conclusion

Dijet production in $e^{\pm}p$ neutral current scattering is investigated in the kinematic range $4 < Q^2 < 80$ GeV^2, $0.1 < y < 0.7$, $x_{I\!P} < 0.03$, $|t| < 1$, $M_Y < 1.6$ GeV, $p^*_{T1} > 5.5$ GeV, $p^*_{T2} > 4.0$ GeV and $-3 < \eta^*_{1,2} < 0$. The cross section is measured deferentially as a function of Q^2, y, $x_{I\!P}$, p^*_{T1}, p^*_{T2}, $\Delta\eta^*$ and $z_{I\!P}$. The integrated cross section at the level of stable hadrons is determined to be

$$\sigma(ep \rightarrow e'X_{dijet}Y) = 63.4 \ \pm \ 0.7 \ (stat) \ \pm \ 6.6 \ (sys) \text{ pb} \tag{6.1}$$

The experimental results are compared to the NLO QCD predictions which are evaluated with the nlojet++ program operated in diffractive regime. The NLO pQCD calculation involving the H1 Fit 2006 B underestimates the measured cross section by about $\sim 12\%$. However, such difference remains within the experimental errors and the uncertainties of the perturbative calculations. Single differential cross sections are found to be in plausible agreement with the NLO QCD prediction. The coincidence between the measured and predicted values of the both integrated and differential cross sections supports the QCD factorization theorem in diffractive DIS processes.

The measured cross sections are further compared to the results of an earlier analysis which studied the dijet production in data collected in years 1999-2000 (period HERA I). The total cross section determined with the HERA I data [46] is lower but agrees with the presented measurement within the experimental uncertainties. The main difference occurs in high $x_{I\!P}$ region that could be biased with a relatively high systematic error in case of the LRG identification of diffraction. It is supported by the fact that the differential dijet cross section in $x_{I\!P}$ agrees rather well with the differential dijet cross section measured for HERA II data where the diffractive events are recognized via the direct proton tagging [47].

The NC DDIS dijet production is measured with unprecedentedly high statistics and provides the input for possibly more precise determination of the diffractive gluon density.

Bibliography

[1] M. Derrick et al. [ZEUS Collaboration]. Observation of events with a large rapidity gap in deep inelastic scattering at HERA. *Phys. Lett. B 315 (1993) 481.*

[2] T. Ahmed et al. [H1 Collaboration]. Deep inelastic scattering events with a large rapidity gap at HERA. *Nucl. Phys. B 429 (1994) 477.*

[3] C. Callan and D. Gross. *Phys. Rev. Lett. 22 156*, 1969.

[4] A. Buras et al. W. Bardeen. Deep-inelastic scattering beyond the leading order in asymptotically free gauge theories. *Phys. Rev. D 18, 3998-–4017*, 1978.

[5] G. 't Hooft and M. Veltman. Regularization and renormalization of gauge fields. *Nucl. Phys. B 44, 189—213*, 1972.

[6] S. Weinberg. New Approach to the Renormalization Group. *Phys. Rev. D 8, 3497–3509*, 1973.

[7] M. Lüscher. Lattice QCD - from Quark Confinement to Asymptotic Freedom. *Annales Henri Poincare 4, 197–210*, 2003.

[8] D. E. Soper et al J. Collins. Perturbative QCD. *Adv. Ser. Direct. High Energy Physics 5, 1*, 1988.

[9] V. N. Gribov and L. N. Lipatov. Deep inelastic ep scattering in perturbation theory. *Sov. J. Nucl. Phys. 15, 438–450*, 1972.

[10] G. Altarelli and G. Parisi. Asymptotic freedom in parton language. *Nucl. Phys. B 126, 298—318*, 1977.

[11] Y. L. Dokshitzer. Calculation of the structure functions for deep inelastic scattering and e^+e^- annihilation by perturbation theory in quantum chromodynamics. *Sov. Phys. JETP 46, 641—653*, 1977.

[12] T. Sjöstrand. In the Proceedings Z physics at LEP. *CERN Yellow Report 89—08.*

[13] A. Donnachie and P. V. Landshoff. Total Cross-Sections. *Phys. Lett., B296:227—232*, 1992.

[14] M. Froissart. *Phys. Rev. 123, 1053*, 1961.

[15] T. Regge. Introduction to Complex Orbital Momenta. *Nuovo Cim., 14:951*, 1959.

[16] T. Regge. Bound States, Shadow States and Mandelstam Representation. *Nuovo Cim., 18:947–956, 1960*, 1960.

[17] J.R. Cudell. The Donnachie–Landshoff pomeron vs. QCD. *hep–ph/9406435*, 1993.

[18] A. B. Kaidalov and Simonov Y. A. *Phys. Lett. B477, 163–170*, 2000.

[19] V. N. Gribov. *JETP Lett. 41, 667–669*, 1961.

[20] J. Collins. Proof of factorization for diffractive hard scattering. *Phys. Rev. D 57 (1998) 3051 [Erratum–ibid. D 61 (2000) 019902] [hep–ph/9709499].*

[21] H1 Collaboration. Measurement and NLO DGLAP QCD Interpretation of Diffractive Deep-Inelastic Scattering at HERA. *ICHEP02, Amsterdam, 980*, 2002.

[22] J. Smith et al. G. Sterman. Handbook of perturbative QCD. *Rev. Mod. Phys. 67, 157–248*, 1995.

[23] Y. Dokshitzer et al. S. Catani. Longitudinally invariant $\mathrm{k_T}$ clustering algorithms for hadron hadron collisions,. *Nucl. Phys. B 406, 187–224*, 1993.

[24] S. Ellis and D. Soper. Successive combination jet algorithm for hadron collisions. *Phys. Rev. D 48, 3160–3166*, 1993.

[25] G. Salam et al. M. Cacciari. The anti-$\mathrm{k_T}$ jet clustering algorithm. *JHEP 04, 063*, 2008.

[26] G. Salam and G. Soyez. A practical seedless infrared-safe cone jet algorithm. *JHEP 05, 086*, 2007.

[27] N. Wainer et al. J. Huth. Toward a standardization of jet definitions. *Research directions for the decade. Summer Study on HEP, Snowmass, Colorado*, 1990.

[28] H. Jung. Hard diffractive scattering in high energy ep collisions and the Monte Carlo generator RAPGAP. *Comput. Phys. Commun. 86, 147–161*, 1995.

[29] S. Mrenna et al. T. Sjöstrand. PYTHIA 6.4 physics and manual. *JHEP 2006, 026*, 2006.

[30] H. Spiesberger et al. A. Kwiatkowski. HERACLES: an event generator for ep interactions at HERA energies including radiative processes. *Comput. Phys. Commun. 69, 155–172*, 1992.

[31] M.H. Seymour S. Catani. A General algorithm for calculating jet cross-sections in NLO QCD. *Nucl.Phys. B485 291–419*, 1997.

[32] Z. Nagy and Z. Trocsanyi. Multijet Cross Sections in Deep Inelastic Scattering at Next-to-Leading Order. *Phys. Rev. Lett. 87, 82001*, 2001.

[33] B. H. Wiik et al. HERA, A Proposal for a Large Electron Proton Colliding Beam Facility at DESY. *DESY-HERA 81/10*, 1981.

[34] I. Abt et al. The H1 detector at HERA. *Nucl. Instr. and Meth. A 386, 310–347*, 1997.

[35] I. Abt et al. The Tracking, calorimeter and muon detectors of the H1 experiment at HERA. *Nucl. Instr. and Meth. A 386, 348–396*, 1997.

[36] B. Denby et al. C. Kiesling. The h1 neural network trigger project. *Advanced computing and analysis techniques in physics research 583, 36–44*, 2001.

[37] A. Schöning. The Fast Track Trigger at the H1 experiment design concepts and algorithms. *Nucl. Instr. and Meth. A 566, 130–132*, 2006.

[38] H. Schultz-Coulon et al. A. Baird. A fast track trigger for the H1 Collaboration. *Nucl. Instr. and Meth. A 461, 461–464*, 2001.

[39] F. Bruyant et al. R. Brun. GEANT: Simulation Program for Particle Physics Experiments. User Guide and Reference Manual. *CERN–DD/EE 84–1*, 1987.

[40] U. Bassler and G. Bernardi. Structure function measurements and kinematic reconstruction at HERA. *Nucl. Instr. Meth. A246 583-598*, 1999.

[41] A. W. Jung. Measurement of the D Meson Cross Section and Extraction of the Charm Contrubution to the Proton Structure in Deep Inelastic Scattering with H1 Detector at HERA. *PhD thesis, University Heidelberg*, 2009.

[42] H1 Collaboration. Measurement of the Diffractive Deep-Inelastic Scattering Cross Section with a Leading Proton at HERA. *DESY 10-095*, 2010.

[43] S.Schmidt. Tunfold, an algorithm for correcting migration effects in high energy physics. *JINST 7, T10003*, 2012.

[44] H1 Collaboration. Diffractive Deep-Inelastic Scattering with a Leading Proton at HERA. *DESY 06-048*, 2006.

[45] S. Schenk. Energy Flow in Hard Diffractive Deep-Inelastic Scattering and Photoproduction with a Leading Proton.

[46] H1 Collaboration. Dijet Cross Sections and Parton Densities in Diffractive DIS at HERA. *DESY 07-115*, 2007.

[47] H1 Collaboration. Measurement of Dijet Production in Diffractive Deep-Inelastic Scattering with a Leading Proton at HERA. *DESY 11-166*, 2011.

[48] H1 Collaboration. Diffractive Deep-Inelastic Scattering with a Leading Proton at HERA. *DESY 06-048*, 2006.